



Available online at [www.sciencedirect.com](http://www.sciencedirect.com)

**ScienceDirect**

Comput. Methods Appl. Mech. Engrg. 366 (2020) 113034

**Computer methods  
in applied  
mechanics and  
engineering**

[www.elsevier.com/locate/cma](http://www.elsevier.com/locate/cma)

# Stress-Particle Smoothed Particle Hydrodynamics: An application to the failure and post-failure behaviour of slopes

C.M. Chalk<sup>a,\*</sup>, M. Pastor<sup>b</sup>, J. Peakall<sup>c</sup>, D.J. Borman<sup>d</sup>, P.A. Sleigh<sup>d</sup>, W. Murphy<sup>c</sup>, R. Fuentes<sup>d,e</sup>

<sup>a</sup> Centre for Doctoral Training in Fluid Dynamics, University of Leeds, LS2 9JT, United Kingdom

<sup>b</sup> ETS de Ingenieros de Caminos, Canales y Puertos, Universidad Politécnica de Madrid, Spain

<sup>c</sup> School of Earth and Environment, University of Leeds, LS2 9JT, United Kingdom

<sup>d</sup> School of Civil Engineering, University of Leeds, LS2 9JT, United Kingdom

<sup>e</sup> Escuela de Ingenieros de Caminos, Canales y Puertos, Universitat Politècnica de València, Spain

Received 27 September 2019; received in revised form 23 March 2020; accepted 23 March 2020

Available online xxxx

## Abstract

We present a new numerical approach in the framework of Smooth Particle Hydrodynamics (SPH) to solve the zero energy modes and tensile instabilities, without the need for the fine tuning of non-physical artificial parameters. The method uses a combination of stress-points and nodes and includes a new stress-point position updating scheme that also removes the need to implement artificial repulsive forces at the boundary. The model is validated for large deformation geomechanics problems, and is able to simulate strain localisation within soil samples and slopes. In particular, the new model produces stable and accurate results of the failure and post-failure of slopes, consisting of both cohesive and cohesionless materials, for the first time.

© 2020 The Author(s). Published by Elsevier B.V. This is an open access article under the CC BY-NC-ND license (<http://creativecommons.org/licenses/by-nc-nd/4.0/>).

**Keywords:** SPH; Stress-points; Dual-particle SPH; Slope behaviour

## 1. Introduction

A detailed understanding of the failure and post-failure of slopes is essential for a number of applications, including ground design and engineering, and landslide risk assessment. Numerical models are invaluable tools that can be utilised to gain insight into slope behaviour — simulations can be performed for a variety of different conditions, allowing a thorough investigation into the physical parameters of interest and how they affect material behaviour. However, the complexity of slope processes means that the development and implementation of such numerical models is far from straightforward. Slope failure is best represented using traditional soil mechanics, whereas its post-failure behaviour shows fluid-like features that require a different framework, typically fluid dynamics [1,2]. The numerical model of choice must therefore be capable of simulating the progressive failure of a solid material, as well as the large deformations and flow-type behaviour associated with post-failure.

\* Corresponding author.

E-mail address: [c.m.chalk@leeds.ac.uk](mailto:c.m.chalk@leeds.ac.uk) (C.M. Chalk).

Mesh-based methods are well established in the field of numerical modelling, and have been applied to simulate problems that are relevant to slope failure [3–6] and post-failure behaviour [7–9]. However, the presence of a mesh poses severe limitations for problems involving large deformations and materials with history-dependent constitutive models. Computationally expensive remedies are required [10]. As an alternative, recent decades have seen a rise in the development of meshless methods. Meshless methods are well suited for modelling large deformation problems, as there is minimal restriction on node displacement. Furthermore, their Lagrangian framework means that meshless models can naturally simulate materials with history-dependency (i.e. stress and strain path dependent), and they have been frequently applied to slope behaviour problems [11–16]. A thorough review of numerical methods (both mesh-based and meshless) with an application to slope behaviour can be found in reference [15]. The oldest meshless method – Smoothed Particle Hydrodynamics (SPH) [17,18] – arguably remains the most popular choice due to the relative simplicity of its implementation [19].

SPH involves the discretisation of a governing system of equations over a set of particles, on which information such as stress and velocity is calculated. The method has been employed to simulate a wide variety of problems regarding slope failure and post-failure, producing promising results [12,20–24]. However, despite the successful applications, it suffers from serious numerical instabilities that are often detrimental to the model performance. Namely, these are: the instability due to *zero-energy modes*, and the *tensile instability*. The former was originally identified in mesh-based methods [25], and occurs when a zero stress gradient is (incorrectly) calculated at individual nodes. Zero-energy modes occur because the stress and velocity are calculated at the same location [26], and they contribute to inaccurate stress and velocity profiles. The effects of this instability are typically most severe when considering solid problems [26,27], and have been documented in SPH simulations of material failure [28,29].

The tensile instability is unique to meshless methods, and occurs in materials with a cohesive strength when subjected to a tensile state of stress. A consequence of the tensile instability is particle clumping, which leads to the development of non-physical material fractures [26,30]. This has been shown to have detrimental effects in simulations involving cohesive soil [20]. Clearly, the effects of zero-energy modes and the tensile instability pose a serious threat to the different stages of slope behaviour. To obtain a universal numerical model, that can be applied to slope failure and post-failure, it is essential that the problems of zero-energy modes and the tensile instability are eliminated from SPH.

There have been numerous attempts to eliminate the tensile instability within SPH. The majority of the proposed solutions are complicated to implement, which counteracts the favourable simplicity of the SPH method. What is more, some of these remedies place restrictions on the movement of the SPH particles — thereby diverging from the true, meshless nature of SPH [27]. Perhaps the most well-known remedy is the artificial stress method [30], which applies a small repulsive force to particles that are in close proximity to one another when under a state of tensile stress. Although the results are effective, the method requires the tuning of artificial, numerical parameters that do not have a physical interpretation. It has also been shown that certain types of kernel function are able to completely eliminate the onset of the tensile instability [27]. However, these types of kernel – Lagrangian kernels – are defined so that the SPH particles have the same neighbours throughout the duration of the simulation. As a result, this method is not appropriate for modelling problems that exhibit large displacements. An alternative numerical scheme was developed for problems in soil dynamics, that is able to combat both the tensile instability and zero-energy modes. The method – Taylor-SPH – combines SPH with the high-accuracy Taylor–Galerkin Finite Elements method [29,31]. This involves two calculation steps that are solved on two different sets of nodes. Taylor-SPH has been applied to simple elastic slopes, the propagation of shear bands, a bearing capacity problem and the slow deformation of a viscoplastic slope. However, the positions of the nodes are somewhat restricted by the two-step calculation, which limits the capabilities regarding high displacement problems. An alternative effective remedy for the tensile instability is the particle shifting technique, where particles in areas of low concentration are shifted accordingly, to eliminate any non-physical fractures [32–34].

In mesh-based methods, zero-energy modes can be completely eliminated by utilising a staggered grid, where stress and velocity are calculated on two separate meshes [35]. Motivated by this, Dyka et al. [36] believed that the same concept could be used to eliminate the tensile instability in SPH, and consequently introduced two sets of particles to SPH in one dimension — nodes and stress-points (see Fig. 1). This method, known as *Stress-Particle SPH*, was able to accurately simulate the previously unsolvable problem of wave propagation in an elastic bar under a state of tensile stress. Stress-points were later included in a two-dimensional Moving Least Squares (MLS) particle method, and used to simulate a number of benchmark problems within solid dynamics [37,38]. A full linear

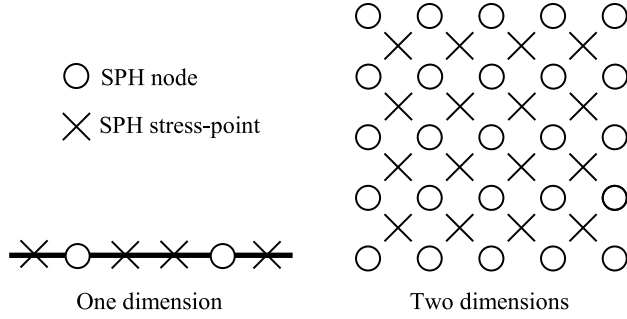


**Fig. 1.** Stress-Particle SPH configurations one and two dimensions.

stability analysis of meshless methods was performed by Belytschko et al. [27], where it was shown that stress-points are capable of completely eliminating zero-energy modes, while also providing stabilisation under tensile states. Subsequently, stress-points were included within the meshless Element-Free Galerkin Method (EFGM) [39–43] and an MLS particle method [44,45] to simulate quasi-static solid problems. In all of the aforementioned studies, stress-points were implemented in meshless methods that are more complex and computationally expensive than SPH. In EFGM for example, a background grid is required for nodal integration, and hence the method is not truly meshless.

Stress-Particle SPH is a stabilised version of SPH that is capable of eliminating both of the detrimental instabilities of the classic SPH method. It removes the instabilities without the need for tuning any artificial parameters. Therefore, the method has the potential to provide a generalised numerical tool that is applicable for all stages of slope behaviour. However, since its introduction, very little attention has been dedicated to this numerical method, despite the initial promising results. In the present investigation, we quantify and analyse the role of stress-points in further detail than has been done before. Furthermore, a long-standing challenge in the implementation of stress-points is the method by which their positions are updated. In Stress-Particle SPH, the nodes carry the material velocity, while the stress-points carry stress information. Therefore, updating the stress-point positions is a non-trivial task, and is the reason why all previous meshless methods with stress-points are restricted to small deformation problems. Here, we develop a novel method of updating the stress-point positions within Stress-Particle SPH, to allow the simulation of large deformation problems (with an application to the post-failure behaviour of slopes). The method consists of assigning two stress-points to follow each node for the duration of the simulation, that are aligned in the direction of the velocity at every node. We show that this approach of arranging and updating the stress-points, named the *velocity vector approach*, produces optimal results regarding the failure and post-failure behaviour of slopes.

The remainder of this paper is structured as follows. In Section 2, we outline the mathematical model used to describe the slope material. Subsequently, in Section 3 we present the governing model equations within the framework of standard SPH, before describing the Stress-Particle SPH method in detail. The results of the Stress-Particle SPH method are provided in Section 4, where we simulate three different problems from the literature that are representative of slope failure. The final problem considered in Section 4 represents the post-failure of a slope. We find that Stress-Particle SPH, in its classic formulation, is unable to simulate the expected flow-type behaviour due to the way in which the stress-points are updated. Consequently, in Section 5 we present an extension of Stress-Particle SPH, which includes the novel technique of updating the stress-point positions. Finally, the key findings of the current investigation, and suggested areas for future work, are provided in Section 6.

## 2. Mathematical description of soil

The equations of motion for a single phase, dry soil consist of the conservation of mass and momentum:

$$\frac{D\rho}{Dt} = -\frac{1}{\rho} \nabla \cdot \mathbf{u}, \quad (1)$$

$$\frac{D\mathbf{u}}{Dt} = \frac{1}{\rho} \nabla \cdot \boldsymbol{\sigma} + \mathbf{b}, \quad (2)$$

where  $\rho$  is the soil density,  $\mathbf{u}$  is velocity,  $\boldsymbol{\sigma}$  is the total stress tensor and  $\mathbf{b}$  denotes the external body forces (consisting of gravity only for the current purposes). Also required is a constitutive equation to relate the soil stresses to the strain rates. We assign a rate-dependent constitutive model to describe the behaviour of soil, according to the theory of plasticity. Under this framework, a material can exhibit both solid and fluid-like behaviour, bridging the gap between the failure and post-failure of soil. Furthermore, the time-dependency of the stress provides history-dependency, allowing the progressive evolution of failure surfaces. Here we present a brief overview of the constitutive model used in the current work — a detailed description can be found in [Appendix A](#).

The fundamental assumption of plasticity is that the total soil strain rate  $\dot{\epsilon}$  can be divided into an elastic and a plastic component

$$\dot{\epsilon} = \dot{\epsilon}^e + \dot{\epsilon}^p, \quad (3)$$

where the superscripts  $e$  and  $p$  denote elastic and plastic strains respectively. Furthermore, we assume a kinematic condition between the total strain rate and the velocity gradients. Here, we consider both a Von Mises and a Drucker–Prager yield criterion to distinguish between elastic and plastic material behaviour.

Regarding the elastic strain rates, we define them according to the generalised Hooke's law for an isotropic material. For the purpose of comparing the results in the current work with those selected from the literature, we consider two alternative definitions for the plastic material behaviour. The first – the elastoplastic model – is based on the theory of classic plasticity and was first implemented within SPH by Bui et al. [20]. The second is the viscoplastic model of Perzyna [46], which contains additional ‘viscous’ terms. This constitutive model was incorporated into the Taylor-SPH method in the work of Blanc [29]. We assume a two-dimensional, plane strain condition, for which the constitutive equation can be written in the following general form

$$\frac{D}{Dt} \begin{pmatrix} \sigma_{xx} \\ \sigma_{yy} \\ \sigma_{xy} \\ \sigma_{zz} \end{pmatrix} = \frac{\partial}{\partial x} \begin{pmatrix} D_{11}^e u_x \\ D_{12}^e u_x \\ D_{33}^e u_y \\ D_{41}^e u_x \end{pmatrix} + \frac{\partial}{\partial y} \begin{pmatrix} D_{12}^e u_y \\ D_{22}^e u_y \\ D_{33}^e u_x \\ D_{42}^e u_y \end{pmatrix} + \begin{pmatrix} g_{xx}^{\epsilon^p}(\dot{\epsilon}^p) \\ g_{yy}^{\epsilon^p}(\dot{\epsilon}^p) \\ g_{xy}^{\epsilon^p}(\dot{\epsilon}^p) \\ g_{zz}^{\epsilon^p}(\dot{\epsilon}^p) \end{pmatrix}, \quad (4)$$

where  $D_{\alpha\beta}^e$ ,  $\alpha, \beta = 1, 2, 3, 4$  is the elastic constitutive tensor in the plane strain condition

$$D_{\alpha\beta}^e = \frac{E}{(1+v)(1-v)} \begin{pmatrix} 1-v & v & 0 & v \\ v & 1-v & 0 & v \\ 0 & 0 & (1-2v)/2 & 0 \\ v & v & 0 & 1-v \end{pmatrix}, \quad (5)$$

and  $E$  and  $v$  denote the Young's modulus and Poisson's ratio respectively. Note that (4) is only valid when material properties do not change. In (4), the final term  $\mathbf{g}^{\epsilon^p} = (g_{xx}^{\epsilon^p}(\dot{\epsilon}^p), g_{yy}^{\epsilon^p}(\dot{\epsilon}^p), g_{xy}^{\epsilon^p}(\dot{\epsilon}^p), g_{zz}^{\epsilon^p}(\dot{\epsilon}^p))^T$  is a function of the plastic strain rates in the constitutive equation, which are non-zero only when the yield function reaches a critical value. The precise form of this term depends on whether the elastoplastic or Perzyna model is implemented. In either case, the plastic strains are functions of stress.

To write (4) in compact form, we define a stress vector  $\boldsymbol{\sigma}$  containing the non-zero components of the stress tensor in plane strain, and introduce the matrix  $\mathbf{f}^u$ :

$$\boldsymbol{\sigma} = \begin{pmatrix} \sigma_{xx} \\ \sigma_{yy} \\ \sigma_{xy} \\ \sigma_{zz} \end{pmatrix}, \quad \mathbf{f}^u = \begin{pmatrix} D_{11}^e u_x & D_{12}^e u_y \\ D_{12}^e u_x & D_{22}^e u_y \\ D_{33}^e u_y & D_{33}^e u_x \\ D_{41}^e u_x & D_{42}^e u_y \end{pmatrix}. \quad (6)$$

Furthermore, we rewrite the equation of momentum in plane strain as

$$\frac{D\mathbf{u}}{Dt} = \frac{1}{\rho} \nabla \cdot \mathbf{f}^{\sigma} + \mathbf{b}, \quad (7)$$

with

$$\mathbf{u} = \begin{pmatrix} u_x \\ u_y \end{pmatrix}, \quad \mathbf{f}^{\sigma} = \begin{pmatrix} \sigma_{xx} & \sigma_{xy} \\ \sigma_{xy} & \sigma_{yy} \end{pmatrix}, \quad \mathbf{b} = \begin{pmatrix} b_x \\ b_y \end{pmatrix}. \quad (8)$$

Finally, the stress rate must be invariant with respect to large body rotations. For this, we replace the standard stress rate with the Jaumann stress rate  $\dot{\hat{\sigma}}$ :

$$\dot{\hat{\sigma}} = \begin{pmatrix} \dot{\sigma}_{xx} \\ \dot{\sigma}_{yy} \\ \dot{\sigma}_{xy} \\ \dot{\sigma}_{zz} \end{pmatrix} - \begin{pmatrix} 2\sigma_{xy}\omega \\ -2\sigma_{xy}\omega \\ (\sigma_{yy} - \sigma_{xx})\omega \\ 0 \end{pmatrix}, \quad \omega = \frac{1}{2} \left( \frac{\partial u_y}{\partial x} - \frac{\partial u_x}{\partial y} \right). \quad (9)$$

Note that the adopted constitutive model is derived under small deformation theory, with the incorporation of (9) to account for large deformations. The objective (i.e. frame invariant) Jaumann stress rate has been shown to exhibit oscillations in simple shear problems, and it may be unsuitable for shear dominated conditions [47]. However its implementation is straightforward, and we find the Jaumann stress rate to be an acceptable assumption — a discussion on alternative objective stress rates can be found in references [47,48].

In summary, the governing mathematical equations for soil in the plane strain condition are written as

$$\text{Conservation of mass : } \frac{D\rho}{Dt} = -\rho \nabla \cdot \mathbf{u}, \quad (10)$$

$$\text{Conservation of momentum : } \frac{Du}{Dt} = \frac{1}{\rho} \nabla \cdot \mathbf{f}^{\sigma} + \mathbf{b}, \quad (11)$$

$$\text{Constitutive equation : } \frac{D\sigma}{Dt} = \tilde{\sigma} + \nabla \cdot \mathbf{f}^u - \mathbf{g}^{\epsilon^p}. \quad (12)$$

where

$$\tilde{\sigma} = \begin{pmatrix} 2\sigma_{xy}\omega \\ -2\sigma_{xy}\omega \\ (\sigma_{yy} - \sigma_{xx})\omega \\ 0 \end{pmatrix}. \quad (13)$$

### 3. Stress-particle SPH

In this section we present the discrete governing equations of soil in the framework of Stress-Particle SPH. First, a brief outline of standard SPH is provided.

#### 3.1. Standard SPH

The derivation of the SPH method consists of two fundamental approximations — the integral approximation and the particle approximation. Detailed reviews on these steps, and the subsequent derivation of various spatial gradient approximations, are in abundance in the SPH literature (a thorough description is provided in reference [19]). Therefore, details on the derivation of the discrete equations within the standard SPH framework are here omitted. Instead, we state the SPH functions of relevance to this work and apply them directly to the mathematical system defined by (10)–(12).

In the framework of SPH, a general function  $f(\mathbf{x})$  is approximated at a particle  $i$  via a summation over the neighbouring particles  $j$ , multiplied by a smoothing function  $W$ :

$$f(\mathbf{x}_i) = \sum_{j=1}^N \frac{m_j}{\rho_j} f(\mathbf{x}_j) W(\mathbf{x}_i - \mathbf{x}_j, h_s). \quad (14)$$

Here,  $m$  is the mass of each particle,  $h_s$  is the smoothing length defining the domain of influence of  $W$ , and  $N$  is the number of neighbouring particles within this domain. The smoothing function, or the kernel, is a continuous function that must satisfy a number of conditions. We employ the popular cubic spline function — a detailed discussion on the smoothing kernel is provided in reference [49]. The gradient of a function can be calculated according to the gradient of the kernel function

$$\frac{\partial f(\mathbf{x}_i)}{\partial \mathbf{x}} = \sum_{j=1}^N \frac{m_j}{\rho_j} (f(\mathbf{x}_j) - f(\mathbf{x}_i)) \frac{\partial W_{ij}}{\partial \mathbf{x}_i}, \quad (15)$$

where  $W_{ij} = W(\mathbf{x}_i - \mathbf{x}_j, h_s) (= W_{ji})$ . Alternatively, a different gradient approximation is often favoured which conserves momentum exactly:

$$\frac{\partial f(\mathbf{x}_i)}{\partial \mathbf{x}} = \rho_i \sum_{j=1}^N m_j \left( \frac{f(\mathbf{x}_i)}{\rho_i^2} + \frac{f(\mathbf{x}_j)}{\rho_j^2} \right) \frac{\partial W_{ij}}{\partial \mathbf{x}_i}. \quad (16)$$

To obtain the discrete system of governing equations, (16) is applied to the stress derivative term in the momentum equation, and (15) is used to discretise the velocity derivative term in the constitutive equation. Here we treat the soil as incompressible, and consequently do not update density via the continuity equation (10). This is not possible in simulations involving fluid dynamics, as density variations are typically required to calculate the fluid pressure via an equation of state [50,51]. In soil mechanics, the soil pressure  $p$  is obtained directly from the equation for hydrostatic pressure:

$$p = -\frac{1}{3} (\sigma_{xx} + \sigma_{yy} + \sigma_{zz}). \quad (17)$$

Note that solving the continuity equation while assuming a constant soil density corresponds to an evolving porosity [20]. The discrete continuity equation is obtained by expanding the velocity gradient term in (10), and applying the SPH derivative approximation (15)

$$\frac{D\rho_i}{Dt} = - \sum_{j=1}^N m_j (\mathbf{u}_j - \mathbf{u}_i) \cdot \frac{\partial W_{ij}}{\partial \mathbf{x}_i}. \quad (18)$$

In the current work, each SPH particle is assigned the same, constant density for the duration of the simulation, and (18) is not explicitly solved unless stated otherwise.

The discrete governing equations of soil motion in the framework of standard SPH are therefore

$$(\text{Conservation of momentum}) \quad \frac{Du_i}{Dt} = \sum_{j=1}^N m_j \left( \frac{\mathbf{f}_i^\sigma}{\rho_i^2} + \frac{\mathbf{f}_j^\sigma}{\rho_j^2} \right) \cdot \nabla W_{ij} + \mathbf{b}_i, \quad (19)$$

$$(\text{Constitutive equation}) \quad \frac{D\sigma_i}{Dt} = \tilde{\sigma}_i + \sum_{j=1}^N \frac{m_j}{\rho_j} (\mathbf{f}_j^\sigma - \mathbf{f}_i^\sigma) \cdot \nabla W_{ij} - \mathbf{g}_i^{\epsilon^p}, \quad (20)$$

where  $\nabla W_{ij} = \frac{\partial W_{ij}}{\partial \mathbf{x}_i}$ . The Jaumann stress rate term is defined as

$$\tilde{\sigma}_i = \begin{pmatrix} 2\sigma_{xy,i}\omega_i \\ -2\sigma_{xy,i}\omega_i \\ (\sigma_{yy,i} - \sigma_{xx,i})\omega_i \\ 0 \end{pmatrix}, \quad (21)$$

and the partial derivatives in  $\omega_i$  are discretised according to the SPH derivative approximation (15).

In addition to the SPH spatial approximation, a time discretisation scheme is also required to update the particle positions in time. We have implemented a fourth order Runge–Kutta scheme (RK4) for this, due to its fourth order accuracy and relatively simple implementation. A description of the time integration of the governing equations with RK4 is provided in [Appendix B](#).

### 3.1.1. Artificial viscosity

The concept of artificial viscosity was introduced by Von Neumann and Richtmyer [52] to model flows with shocks. The meshless nature of SPH means that the effects of shocks are more severe than for mesh-based methods — they induce irregular particle motions on the length scale of the initial particle separation, and result in large pressure fluctuations. An adapted artificial viscosity was implemented within SPH to dampen the irregular particle motion and pressure fluctuations, and to prevent non-physical collisions of two approaching particles [53]. The artificial viscosity term  $\Pi_{ij}$  is included in the SPH momentum equation as:

$$\frac{Du_i}{Dt} = \sum_{j=1}^N m_j \left( \frac{\mathbf{f}_i^\sigma}{\rho_i^2} + \frac{\mathbf{f}_j^\sigma}{\rho_j^2} + \Pi_{ij} \mathbf{I} \right) \cdot \nabla W_{ij} + \mathbf{b}_i, \quad (22)$$

where  $\mathbf{I}$  is the identity matrix. The most widely used form of artificial viscosity is

$$\Pi_{ij} = \begin{cases} \frac{-\alpha_\Pi c_{ij} \phi_{ij} + \beta_\Pi \phi_{ij}^2}{\rho_{ij}}, & \mathbf{u}_{ij} \cdot \mathbf{x}_{ij} < 0 \\ 0, & \mathbf{u}_{ij} \cdot \mathbf{x}_{ij} \geq 0 \end{cases} \quad (23)$$

$$\phi_{ij} = \frac{h_{sij} \mathbf{u}_{ij} \cdot \mathbf{x}_{ij}}{|\mathbf{x}_{ij}|^2 + 0.01 h_{sij}^2}, \quad c_{ij} = \frac{c_i + c_j}{2}, \quad \rho_{ij} = \frac{\rho_i + \rho_j}{2}, \quad (24)$$

$$h_{sij} = \frac{h_{si} + h_{sj}}{2}, \quad \mathbf{x}_{ij} = \mathbf{x}_i - \mathbf{x}_j, \quad \mathbf{u}_{ij} = \mathbf{u}_i - \mathbf{u}_j. \quad (25)$$

where  $\alpha_\Pi$  and  $\beta_\Pi$  are problem dependent tuning parameters and  $c$  is the speed of the sound. The latter is dependent upon the material under consideration, which for a soil lies between 450–600 m/s [54,55]. The term  $0.01 h_{sij}^2$  is included to prevent numerical divergence when two particles approach one another. Note that the pressure fluctuations discussed above should be distinguished from the instabilities associated with the zero-energy modes and tensile instability. While the artificial viscosity is also able to reduce the effects of these instabilities, it is unable to eliminate them fully. Furthermore, a high value of artificial viscosity can produce excessive material shear strength and non-physical stiffness [26].

### 3.2. Stress-particle SPH

In the Stress-Particle SPH method there are two sets of particles — nodes and stress-points. The velocity is calculated on the SPH nodes and the stress is calculated on the stress-points. The discrete equations in Stress-Particle SPH take the same form as those defined by (19) and (20). The difference is that the momentum equation (19) is solved on the SPH nodes, utilising stress information (to obtain  $\mathbf{f}^\sigma$ ) from the neighbouring stress-points (as opposed to the neighbouring nodes). The velocity is therefore updated and stored on the SPH nodes. Meanwhile, the constitutive equation (20) is solved on the SPH stress-points in order to update the stress. Velocity information (to calculate  $\mathbf{f}^u$ ) is utilised from the neighbouring nodes. Within the framework of Stress-Particle SPH, the subscripts  $i$  and  $j$  in (19) and (20) no longer both refer to SPH nodes —  $i$  refers to the nodes, while  $j$  refers to the stress-points. In this framework, the governing equations are written as

$$(\text{Calculated on node } i) \quad \frac{D\mathbf{u}_i}{Dt} = \sum_{j=1}^N m_j \left( \frac{\mathbf{f}_i^\sigma}{\rho_i^2} + \frac{\mathbf{f}_j^\sigma}{\rho_j^2} \right) \cdot \nabla W_{ij} + \mathbf{b}_i, \quad (26)$$

$$(\text{Calculated on stress-point } j) \quad \frac{D\sigma_j}{Dt} = \tilde{\sigma}_j + \sum_{i=1}^N \frac{m_i}{\rho_i} (\mathbf{f}_i^u - \mathbf{f}_j^u) \cdot \nabla W_{ji} - \mathbf{g}_j^{\epsilon^p}, \quad (27)$$

where  $\nabla W_{ji} = -\nabla W_{ij}$ . The RK4 scheme is applied to integrate (26) and (27) in time, in the same way as for standard SPH (see Appendix B). Furthermore, artificial viscosity can also be incorporated into (26), as described earlier. Node-node interactions (as opposed to node-stress-point) are utilised to obtain the artificial viscosity terms.

The discrete variable gradient terms on the right hand side of Eqs. (26) and (27) involve the value of that variable at the particle itself. For example, the divergence of  $\mathbf{f}^\sigma$  at node  $i$  in (26) is approximated as:

$$(\nabla \cdot \mathbf{f}^\sigma)_i = \sum_{j=1}^N m_j \left( \frac{\mathbf{f}_i^\sigma}{\rho_i^2} + \frac{\mathbf{f}_j^\sigma}{\rho_j^2} \right) \cdot \nabla W_{ij}, \quad (28)$$

which requires the value of  $\mathbf{f}^\sigma$  at node  $i$  (in addition to the values of  $\mathbf{f}^\sigma$  at the surrounding stress-points  $j$ ). The matrix  $\mathbf{f}^\sigma$  is a function of stress, which is stored on the stress-points. Therefore, in order to calculate  $\mathbf{f}^\sigma$  at the nodes, the stress must be transferred from the surrounding stress-points. Similarly, values of  $\mathbf{f}^u$  (which is a function of velocity) are required at the stress-points to approximate the divergence of  $\mathbf{f}^u$  in (27). Thus, the velocity must be transferred from the nodes to the stress-points. The method in which the stress and velocity are interpolated onto the nodes and stress-points is an important aspect of Stress-Particle SPH.

In the one-dimensional Stress-Particle set-up introduced by Dyka et al. [36] (depicted in Fig. 1), the stress at each node is approximated as being the average of the two stress-points on either side. Meanwhile, the velocity of each pair of stress-points is defined to be equal to that of their intermediate node. In two dimensions, the transfer of the

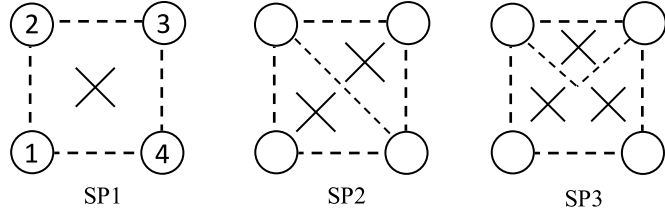


**Fig. 2.** Examples of different node–stress-point arrangements, with one, two and three stress-points inside each virtual quadrilateral.

stress to the nodes and the velocity to the stress-points is more complex. In all previous particle-based methods with the implementation of stress-points, the variable interpolation was performed via an MLS approximation [27,37–39,41]. MLS approximations are shape functions, that attempt to minimise the sum of the squared deviations of a function from existing data points. It is linearly consistent, but considerably more complex to construct than the SPH smoothing kernel. In the current work, we employ a simple interpolation method to transfer the information between the nodes and stress-points. The interpolation utilises the SPH function approximation, with the Corrective Smoothed Particle Method (CSPM) normalisation technique [56] to reduce the truncation errors near the material boundaries, as well as to eliminate the dependency of the interpolation procedure on the particle mass. Thus, the velocity and stress are transferred onto the stress-points and nodes respectively as

$$\boldsymbol{u}_j \approx \frac{\sum_{i=1}^{N_i} \frac{m_i}{\rho_i} \boldsymbol{u}_i W_{ij}}{\sum_{i=1}^{N_i} \frac{m_i}{\rho_i} W_{ij}}, \quad (29)$$

$$\boldsymbol{\sigma}_i \approx \frac{\sum_{j=1}^{N_j} \frac{m_j}{\rho_j} \boldsymbol{\sigma}_j W_{ij}}{\sum_{j=1}^{N_j} \frac{m_j}{\rho_j} W_{ij}}, \quad (30)$$

where  $N_i$  denotes the number of nodes within the neighbourhood of each stress-point, and  $N_j$  denotes the number of stress-points within the neighbourhood of each node.

### 3.3. Node–stress-point arrangement

The stabilising effects of stress-points within SPH are dependent on the initial node–stress-point arrangement [27]. In this work, we initially consider three node–stress-point configurations, where a specified number of stress-points are placed inside virtual quadrilaterals. The different configurations are depicted in Fig. 2, and consist of one, two and three stress-points placed inside every virtual quadrilateral. These three configurations are denoted SP1, SP2 and SP3 respectively. To describe in further detail the locations of the stress-points, the four nodes are labelled 1,2,3 and 4 — starting from the bottom left node and moving clockwise to the bottom right node. The stress-point in configuration SP1 is simply placed in the centre of nodes 1,2,3 and 4. The SP2 configuration includes two stress-points, with each one placed in the centre of the two ‘virtual triangles’ that are created by connecting the nodes 2 and 4. The SP3 configuration includes three stress-points that are positioned as follows. One is placed in the centre of the virtual triangle made by connecting nodes 1,2 and 4. The second stress-point is placed in the centre of the virtual triangle made by connecting nodes 1, 3 and 4. Finally, the third stress-point is positioned in the centre of the triangle created by connecting nodes 2 and 3 with the centre of the quadrilateral.

In their stability analysis, Belytschko et al. [27] explored a variety of node–stress-point arrangements, and found that the least stable configuration was to have one stress-point positioned in the centre of every virtual quadrilateral (the SP1 configuration). Until now, all two-dimensional meshless models with stress-points have only considered this simple configuration.

### 3.4. Particle position update

In standard SPH, the simplest way in which to update each particle position is to calculate the displacement:

$$\frac{d\mathbf{x}_i}{dt} = \boldsymbol{u}_i. \quad (31)$$

Eq. (31) is updated from time  $t$  to  $t + \Delta t$  as

$$\mathbf{x}_i^{t+\Delta t} = \mathbf{x}_i^t + \Delta t \mathbf{u}_i^{t+\Delta t/2}, \quad (32)$$

where  $\Delta t$  is the time increment and  $\mathbf{u}_i^{t+\Delta t/2}$  is the average of the velocity at the current time and the previous time.

Unless stated otherwise, (32) is solved to move the SPH nodes in the current work. Updating the positions of the stress-points is less straightforward, because the material velocity is not calculated on these particles. Nonetheless, they do have a velocity that is interpolated from the surrounding nodes (as required for the calculation of the velocity gradient on the stress-points). Hence, one way in which to update the stress-point positions is according to this interpolated velocity, and applying (32) in the same way as for the nodes. This method has been used to update the stress-point positions in all existing stress-point schemes in the literature. Until now, all applications of the Stress-Particle method have been confined to small displacement problems, and this method has been sufficient. We initially apply (32) to move the stress-points in this work. However, as shall be seen in Section 4.3.2, this method is unsuitable for problems involving rapid velocities and large displacements. This has motivated the extension of Stress-Particle SPH for large displacement problems, introduced in Section 5. It should be noted that the overlap of two stress-points has no detrimental effect on the simulation — both stress-points simply have an equal influence on the surrounding nodes. Similarly, if a stress-point overlaps a node the SPH discretisation method ensures that the stress-point has no influence on the node in question. Therefore, no special technique is required to prevent the overlap of two stress-points (or a node and a stress-point).

### 3.5. Boundary treatment

It follows from the meshless nature of SPH that the treatment of boundary conditions is non-trivial. For methods that involve a mesh, the boundary condition can be simply applied to the relevant nodes. This can also be performed in SPH simulations when the node positions are not updated, or if the particle displacement is small. This simple boundary treatment is implemented in the current work for the low displacement problems under consideration. To reduce the errors associated with the kernel truncation near the boundaries, the CSPM normalisation method is applied to the gradient terms in the governing equations. Details of this can be found in Appendix C.

In many applications, wall boundaries are required within SPH simulations. Here, we require no-slip walls for the cohesive and non-cohesive soil failure simulations (see Section 4.3). For this, we incorporate dummy nodes — layers of SPH particles that interact with interior particles to simulate a no-slip condition. This method was introduced by Morris et al. [57] to model incompressible flows, and adapted by Bui et al. [20] to be suitable for soil dynamics problems. A complete description of the method for standard SPH can be found in reference [20]. Here, we describe the dummy node method (for straight, stationary walls) with an application to Stress-Particle SPH.

The wall boundary is represented by three layers of dummy nodes, spaced apart by the initial particle spacing  $\Delta x$ , as represented by the filled circles in Fig. 3. The first layer of dummy nodes is positioned at the location of the wall itself, which is at a distance  $\Delta x$  away from the inner most interior particles. For an interior particle  $A$  (node or stress-point) that contains a dummy node  $B$  within its neighbourhood, the normal distances  $d_A$  and  $d_B$  (of  $A$  and  $B$  respectively) to the wall are calculated. An artificial velocity  $\mathbf{u}_B$  is then assigned to the dummy particle:

$$\mathbf{u}_B = -\frac{d_B}{d_A} \mathbf{u}_A, \quad (33)$$

where  $\mathbf{u}_A$  is the velocity of the interior node. To account for extremely large values of the dummy node velocity when an interior particle approaches the boundary (and  $d_A$  approaches zero), a parameter  $\beta$  is introduced:

$$\mathbf{u}_B = (1 - \beta) \mathbf{u}_A + \beta \mathbf{u}_{wall}, \quad \beta = \min \left( \beta_{\max}, 1 + \frac{d_B}{d_A} \right), \quad (34)$$

where optimum values of  $\beta_{\max}$  have been found to be between 1.5 — 2 [20,57]. Here we use  $\beta = 1.5$ . The velocities of the dummy nodes are then included in the calculation of the velocity gradient at the interior particles to apply the no-slip effect. In standard SPH the velocity gradient is calculated on the SPH nodes (via the  $\mathbf{f}'$  term) when solving the constitutive law. Conversely, for Stress-Particle SPH, the velocity gradient is calculated on the stress-points, and the no-slip effect is consequently applied via the stress-points, instead of the nodes (via the stress-point–dummy node interaction). We found that this indirect application of the no-slip condition does not always guarantee that the

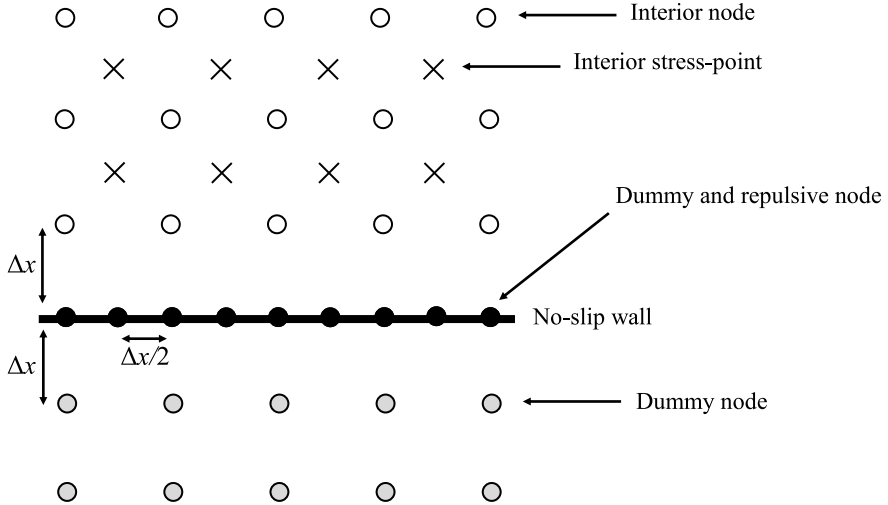


**Fig. 3.** A schematic depiction of the dummy nodes and their interaction with the interior particles for Stress-Particle SPH (configuration SP1).

nodes do not penetrate the wall boundary. Therefore, we also apply a soft repulsive force [58] to the nodes near the wall boundary, which is incorporated as a body force in the momentum equation. The force is applied via a layer of repulsive particles located at the wall boundary, spaced apart by a distance of  $\Delta x/2$ . These repulsive particles are included as black filled circles on the schematic diagram in Fig. 3. Note the particles that lie on the boundary itself are both dummy nodes and repulsive nodes. The definition of the repulsive force is provided in Appendix D.

For the application of SPH to a rate-dependent soil, it is also necessary to assign stress values to the dummy nodes. Following Bui et al. [20], for a pair of interacting interior nodes and dummy nodes (denoted as  $A$  and  $B$  respectively), the stress of the boundary particle is defined to be equal to the stress of the interior node:

$$\sigma_B = \sigma_A. \quad (35)$$

This simple definition ensures that there is a uniform stress distribution for the nodes that are near the wall boundaries, and it contributes to smooth stress distributions in these areas. The boundary stress values defined by (35) are included in the stress gradient calculations (through the  $\mathbf{f}^\sigma$  term) on the interior nodes in the equation of momentum (through the node–dummy node interaction).

In free surface problems the nodes that comprise the free surface should satisfy a stress-free condition. When considering large deformations this first requires the detection of free surface particles, followed by a transformation of the stress tensor so that the normal and tangential components are zero [29]. In the current investigation this procedure is only relevant to the free surface problem described in Section 4.3.

#### 4. Stress-particle SPH: validation results

The Stress-Particle SPH method has been applied to a variety of problems within geomechanics, utilising both the elastoplastic and the Perzyna constitutive model. It should be noted that in the elastoplastic model, the stress state is not allowed to exceed the yield surface. However, this is not guaranteed in the numerical implementation unless a corrective treatment is applied. The stress must therefore be checked at every calculation step and adapted if it does not lie within a valid range. This technique was developed by Chen et al. [3] for the numerical modelling of soil in an FEM model, and was also used within SPH by Bui et al. [20] for the simulation of a soil with a Drucker–Prager yield surface. A full description of this treatment can be found in reference [20]. We apply this stress adaptation to both nodes and stress-points, after every calculation step.

In this section we compare the results obtained with Stress-Particle SPH to those of the standard SPH model. The different node–stress-point arrangements – SP1, SP2 and SP3 – are investigated and analysed. First, we consider the simple problem of an elastic vertical slope (where the  $\mathbf{g}^{\epsilon^p}$  term in the constitutive equation is neglected). We

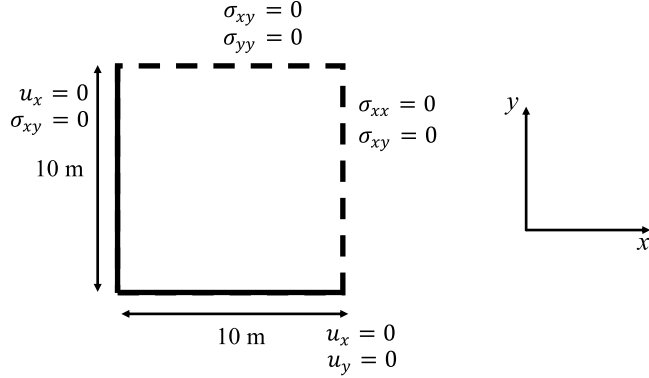


**Fig. 4.** A schematic diagram of the vertical slope.

compare these results to those obtained with the Taylor-SPH model, presented in reference [29]. Next, we simulate the shear band development in a Perzyna soil sample, with strain softening behaviour. Finally, we model the failure of a cohesive and non-cohesive elastoplastic soil — a problem first introduced by Bui et al. [20].

#### 4.1. Elastic vertical slope

The elastic vertical slope consists of an initial soil square with sides of 10 m that is allowed to deform under the effects of gravity. This problem was simulated by Blanc [29] and Blanc and Pastor [31] with the Taylor-SPH model, 441 SPH nodes spaced apart by  $\Delta x = 0.5$  m, and a time step of  $\Delta t = 0.001$  s. In order to completely eliminate stress and velocity oscillations, a damping coefficient of  $\mu_d = 50$  was included in the momentum equation. The damping coefficient provides an alternative way of reducing inter-particle fluctuations (instead of the artificial viscosity), and is incorporated by including the term  $-\mu_d \mathbf{u}$  as a body force. Furthermore, the gravitational force was applied progressively over one second, to remove the fluctuations resulting from the application of this loading. Due to the relatively low displacement observed in the problem, Blanc [29] did not update the positions of the nodes and the boundary conditions were explicitly enforced on the boundary nodes (see Fig. 4 for a schematic diagram). Note that the damping coefficient may reduce the severity of numerical instabilities within SPH, but cannot eliminate them completely. A coefficient that is too large results in unrealistic material behaviour.

We have used the same input conditions in the current standard SPH and Stress-Particle SPH models, with a smoothing length of  $h_s = 0.8\Delta x$ . The particle positions were also not updated, and the boundary conditions were explicitly enforced on the boundary particles, with the CSPM normalisation applied to the stress and velocity gradient approximations. The Young's modulus, Poisson's ratio and material density are  $8 \times 10^7$  Pa, 0.3 and  $2000 \text{ kg/m}^3$  respectively.

Contours of stress and displacement after 2 s of simulation are provided in Fig. 5, comparing the Taylor-SPH results with those of standard SPH and Stress-Particle SPH. The displacement  $s$  is calculated according to  $\mathbf{u} = \frac{ds}{dt}$ . The vertical stress profile provided by Blanc [29] exhibits the expected behaviour of an increase in compressive stress with sample depth, including a disturbance near the right boundary due to the interaction between the stress-free and the no-slip boundaries. The horizontal stresses are negative in the bottom left corner and increase towards a positive value at the top of the sample, due to the gradual horizontal movement under the effects of gravity. The total displacement is largest at the top of the sample, and smoothly decreases to a value of zero at the bottom. This general behaviour is captured with both Stress-Particle SPH and standard SPH. The results of SP2 and SP3 show slight differences to those of the Taylor-SPH model — there is a small discontinuity at the left boundary in the stress profiles. Furthermore, the SP3 results show extra discontinuities in the vertical stress profile at the bottom boundary. As the stress-points lie closer to the boundaries in the SP2 and SP3 set-ups than in SP1, we suggest that these discrepancies are related to the boundary-stress-point interaction. The results of standard SPH exhibit severe singularities in stress and displacement, which are typical manifestations of the zero-energy modes. This is despite the inclusion of a damping force and the progressive application of gravity, which have been previously shown to reduce stress fluctuations in SPH [59]. The singularities have been completely eliminated with Stress-Particle

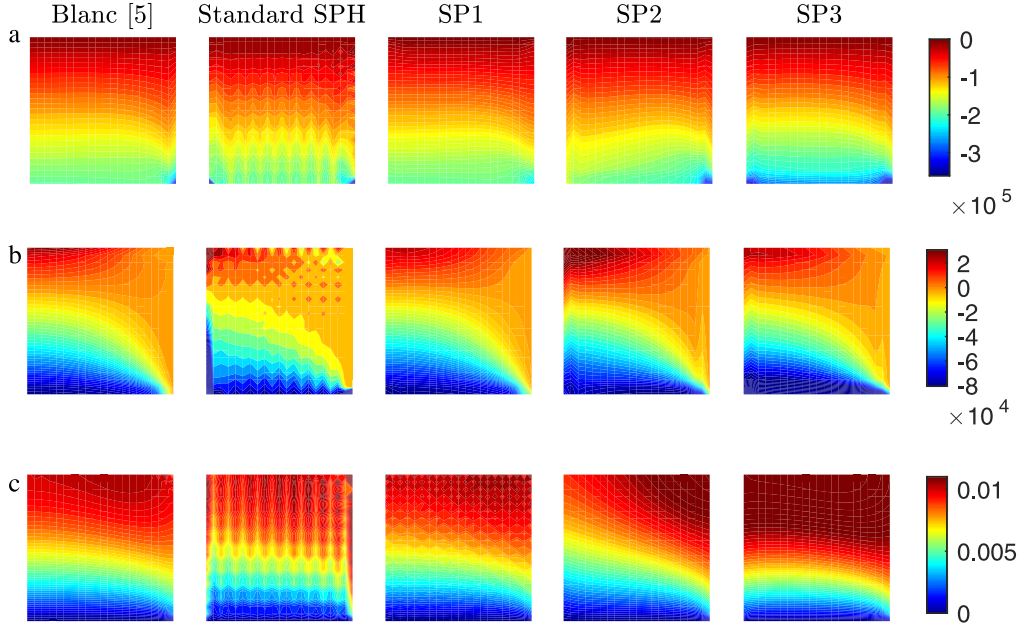


**Fig. 5.** Contours of stress and velocity in the elastic slope at  $t = 2$  s, comparing the standard SPH and Stress-Particle SPH results with those of Blanc [55]. (a) Vertical stress  $\sigma_{yy}$  (Pa) (b) Horizontal stress  $\sigma_{xx}$  (Pa) (c) Total displacement  $|s| = \sqrt{s_x^2 + s_y^2}$  (m)

SPH with configurations SP2 and SP3. While the singularities are not present in the stress profiles of the SP1 configuration, the displacement contours exhibit small oscillations, suggesting that the zero-energy modes were not eliminated completely.

#### 4.2. Strain localisation in a soil sample with strain softening

We have applied our SPH model to simulate the strain localisation in a soil sample, described with a viscoplastic Perzyna constitutive model. A Von Mises yield criterion was included, and the yield surface  $Y$  (Pa) was defined to vary according to a softening law:

$$\frac{DY}{Dt} = H \frac{D\bar{\epsilon}^P}{Dt}. \quad (36)$$

Here  $H$  is a hardening modulus (Pa) and  $\bar{\epsilon}^P$  is the deviatoric plastic strain (which represents the magnitude of plastic strain):

$$\bar{\epsilon}^P = \sqrt{(2\epsilon_{xx}^P)^2 + (2\epsilon_{yy}^P)^2 + (2\epsilon_{zz}^P)^2 + (\epsilon_{xy}^P)^2} / 3 \quad (37)$$

The material parameters are provided in Table 1. We simulated half of a square sample with a 1 m side, with a symmetry condition applied to the left boundary (see Fig. 6). The resultant shock wave propagated through the sample and produced irreversible deformations, which localised as a shear band. This problem was previously considered by Mabssout and Herreros [60] with the Taylor-SPH method, although in a plane stress condition. In their results, the shear band propagated at an inclination angle of 35°, which agrees with the theoretical solution for a Von Mises material in the plane stress condition [61]. Here, we assume a plane strain condition, for which the theoretical angle is calculated to be 45°.

A tensile force was applied by imposing a vertical upwards velocity on the upper boundary, which makes the SPH model highly susceptible to the tensile instability. Mabssout and Herreros [60] employed a Lagrangian kernel within Taylor-SPH to eliminate all instabilities. The boundary conditions shown in Fig. 6 were applied directly to the SPH boundary nodes, with the CSPM gradient normalisation. The time step and smoothing length were  $\Delta t = 1 \times 10^{-5}$  s and  $h_s = 1.2\Delta x$  respectively, with 3321 particles spaced  $\Delta x = 0.0125$  m apart.

**Table 1**

Material parameters for the strain localisation problem.  $Y_0$  is the initial size of the yield surface, and  $\gamma$  and  $\hat{N}$  are Perzyna model parameters — the latter is the plastic strain exponent, while the former is the fluidity parameter.

$E$ (Pa)	$H$ (Pa)	$H/E$	$\rho$ (kg/m <sup>3</sup> )	$Y_0$ (Pa)	$\gamma$ (1/s)	$\hat{N}$
$8 \times 10^7$	$-8 \times 10^6$	-1/10	2000	$5 \times 10^5$	50	1

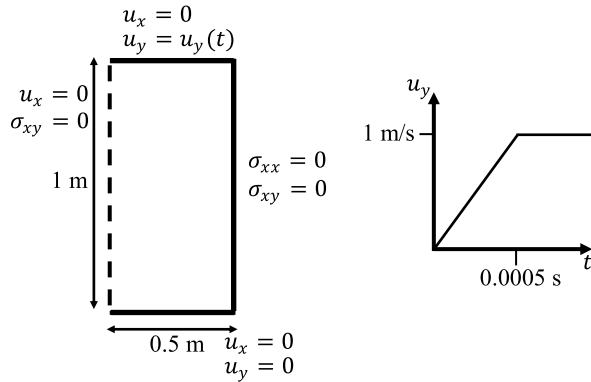


**Fig. 6.** A schematic diagram of the strain localisation problem, with the imposed velocity profile for the upper boundary.

Contours of deviatoric plastic strain are provided in Fig. 7a for standard SPH (with and without artificial viscosity), SP1, SP2 and SP3 (with no artificial viscosity for the latter three). All three configurations of the Stress-Particle method display well-defined shear bands at  $t = 0.02$  s, that have an approximate inclination angle of  $45^\circ$ . The shear stress profiles shown in Fig. 7b are also smooth for all configurations of Stress-Particle SPH. Regarding standard SPH, it was essential to include artificial viscosity with relatively large values of the input parameters ( $\alpha_\pi = \beta_\pi = 0.5$ ) to obtain a stable solution. As can be seen in Fig. 7, it was not possible to simulate any shear band development with standard SPH without artificial viscosity. However, the addition of artificial viscosity results in excessive material shear strength. This is evident from the horizontal stripes displayed in the shear stress contours. Furthermore, the excessive strength has inhibited the propagation of the shear band in the upper half of the soil sample. Effects of artificial shear strength due to the artificial viscosity were first identified by Swegle et al. [26] in the simulation of two impacting metal plates. The artificial viscosity acts to reduce particle fluctuations relative to one another — Swegle et al. [26] discovered that this inhibition of relative particle motion can cause the SPH particles to form ordered chains, which provided the metal plates with extra, unrealistic strength.

#### 4.3. Large elastoplastic vertical slope

Here we present simulations of the soil failure problem introduced by Bui et al. [20]. The problem consists of a perfectly plastic, elastoplastic material that is allowed to collapse and deform under the effects of gravity. A Drucker–Prager yield function was used to describe the soil, of which the key model parameters are the material cohesion  $c_{oh}$  and the angle of internal friction  $\phi$ . Bui et al. [20] simulated the problem with SPH, both with and without cohesion. The material has an initial rectangular area of 4 m in length and 2 m in height and is constrained by no-slip walls (composed of dummy nodes) at the left and bottom boundaries. 5000 uniformly distributed SPH nodes were used to describe the material, with a time step of  $\Delta t = 1.5 \times 10^{-5}$  s, a smoothing length of  $h_s = 1.2\Delta x$  and an initial particle spacing of  $\Delta x = 0.04$  m. Bui et al. [20] also included artificial viscosity with parameters  $\alpha_\Pi = \beta_\Pi = 0.1$  and a speed of sound of  $c = 600$  m/s. The material parameters are provided in Table 2. It should be noted that, following Bui et al. [20], no stress-free boundary condition was applied to the free-surface nodes. This was found to have little effect on the material deformation and evolution.

In the case of the cohesive soil, severe non-physical fractures were exhibited due to the tensile instability unless a stabilisation technique was employed. For this, Bui et al. [20] included the artificial repulsive force [30]. We have also implemented the artificial stress within our standard SPH model, to compare its ability at removing the tensile

**Table 2**

Drucker–Prager material parameters for the cohesive and non-cohesive soil failure.

$E$ (Pa)	$\rho$ (kg/m <sup>3</sup> )	$c_{oh}$ (Pa)	$\phi$ (°)
$1.8 \times 10^6$	1850	5000	25

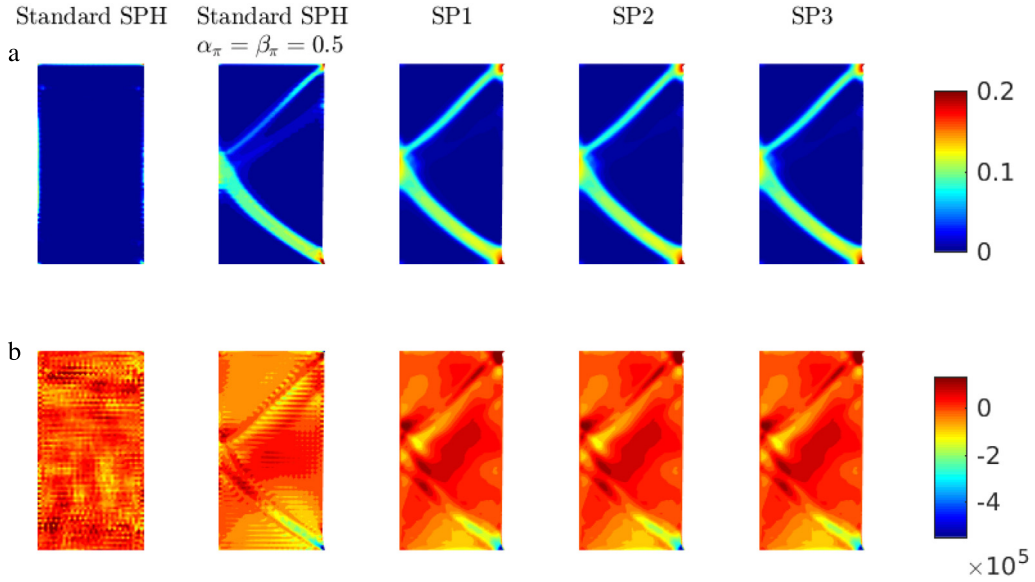


**Fig. 7.** A comparison of deviatoric plastic strain, stress and velocity profiles for the strain localisation problem at  $t = 0.02$  s, for standard SPH, SP1, SP2 and SP3. (a) Deviatoric plastic strain  $\bar{\epsilon}^P$  (dimensionless) (b) Shear stress  $\sigma_{xy}$  (Pa)

instability with that of Stress-Particle SPH (see Appendix E for detail on the artificial stress implementation). The final run-out position of both the cohesive and non-cohesive materials are provided in Fig. 8, comparing the results from our standard SPH model with those of Bui et al. [20]. It can be seen that the free surface profiles align closely in both cases. The majority of the model conditions used by Bui et al. [20] have been employed in the current application, in an attempt to recreate their results as closely as possible. The exceptions are as follows: Bui et al. [20] used a second order leapfrog time integration method, and updated the soil density according to the continuity equation. We have utilised an RK4 scheme, and have not updated the continuity equation — we found that updating the density has a negligible effect on the SPH results (see Fig. 8).

#### 4.3.1. Cohesive soil

The progressive failure of the cohesive soil is shown in Fig. 9, computed with standard SPH with and without the artificial stress, SP1 and SP2. The material is coloured by the deviatoric plastic strain, which first appears in the bottom right corner of the material due to the interaction between the moving nodes and the no-slip boundary. The slope progressively fails as the region of irreversible deformation localises as a shear band and propagates through the sample, forming the failure surface. For standard SPH, non-physical fractures first appear in the soil at  $t = 0.6$  s, which grow more severe with time. As also shown by Bui et al. [20], the artificial stress suppresses the effects of the tensile instability, and the corresponding results do not exhibit any non-physical fractures. We can see that the material fracture has also been eliminated with the Stress-Particle SPH model, for both SP1 and SP2. The SP3 results were almost identical to those of SP2, and they are therefore not shown here. Note that repulsive boundary particles were included within Stress-Particle SPH to prevent the penetration of the interior nodes through the wall. In the profiles of standard SPH (with the artificial stress), the shear band is composed of two thinner bands that both originate from the bottom right corner. These two separate bands are not as distinguished in the Stress-Particle SPH results, indicating that the method has smoothed over this detail. The SP1 results show some additional regions

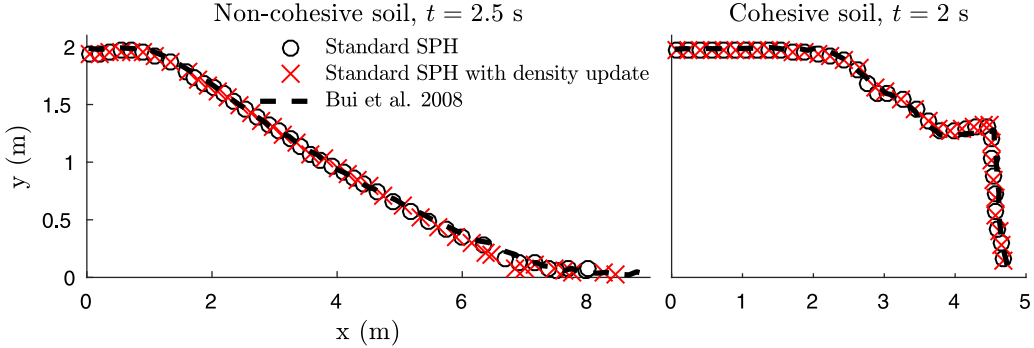


**Fig. 8.** The final material position in the cohesive and non-cohesive soil failure simulations, comparing the results of the current standard SPH model (circles and crosses) with those provided by Bui et al. [62] (dashed line). The red crosses depict the results when the density was updated according to the discrete continuity equation (18). Note that the artificial stress was included in the cohesive soil simulation.

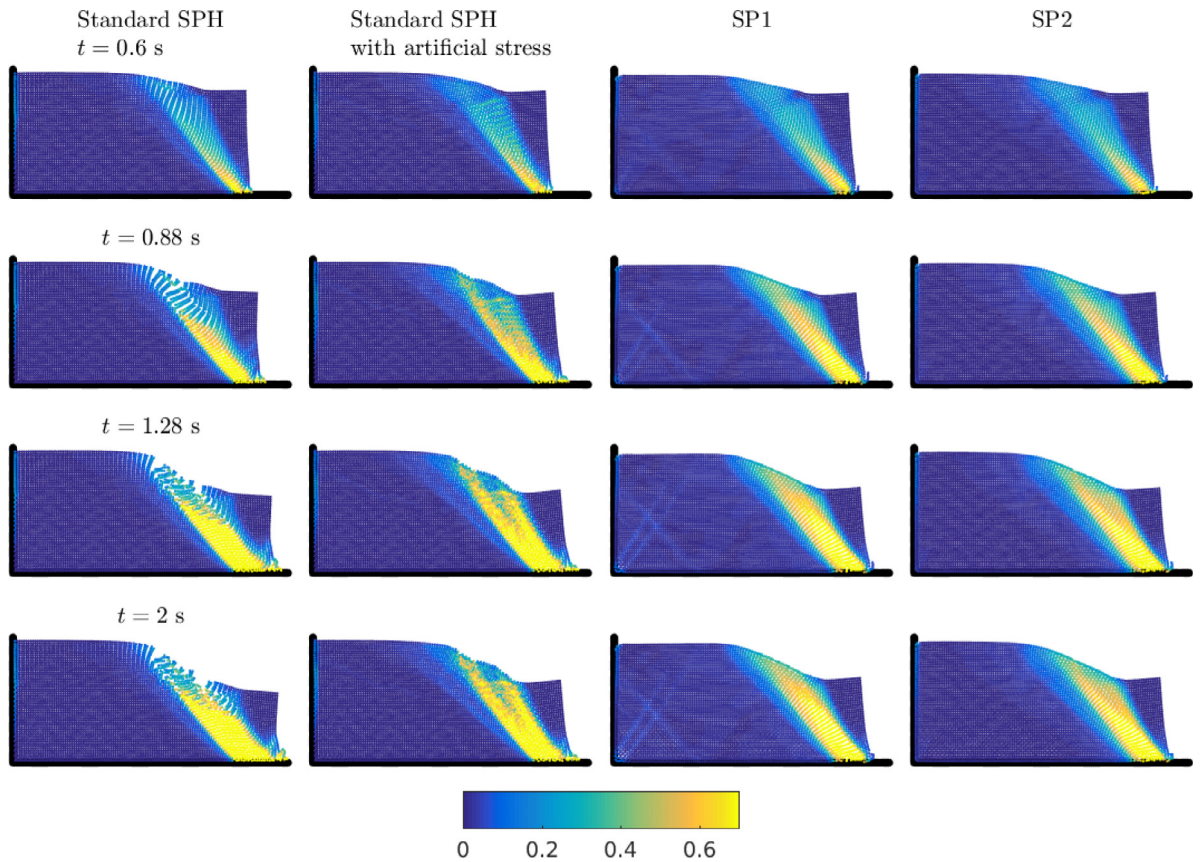


**Fig. 9.** Snapshots of the progressive failure of the cohesive soil, for standard SPH, standard SPH with the artificial stress [13], SP1 and SP2. The material is coloured by values of deviatoric plastic strain  $\bar{\epsilon}^p$  (dimensionless)

of localised plastic strain close to the intersection between the two walls, suggesting that the material has slipped along the wall. It is possible that there are not enough stress-points within the neighbourhood of the dummy nodes to effectively simulate the no-slip effect for configuration SP1.

The final node positions (coloured by vertical stress) are compared in Fig. 10 for standard SPH with the artificial stress and the Stress-Particle SP2 method. The nodes in the region of the tensile instability are shown in detail. The results of standard SPH exhibit a noisy stress profile, particularly along the region of the shear band. Stress-Particle

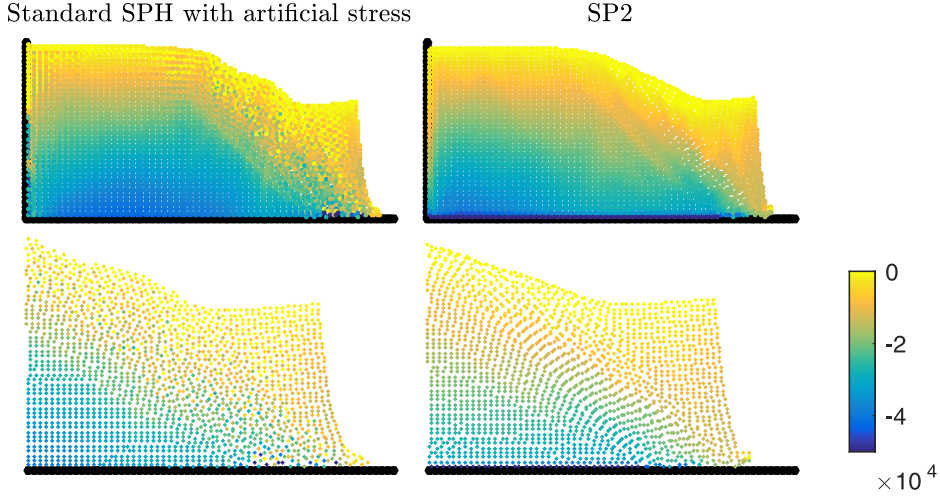


**Fig. 10.** Node positions at the end of the cohesive soil failure problem ( $t = 2$  s), for standard SPH with the artificial stress, and Stress-Particle SPH with the SP2 configuration. The nodes are coloured by values of vertical stress  $\sigma_{yy}$  (Pa).

SPH has produced a notably smoother stress profile, with no obvious fluctuations. The smooth profiles are a result of the interpolation process in the Stress-Particle method — the stress at each node is calculated via a normalised SPH interpolation over the surrounding stress-points (according to Eq. (30)). Concerning the structure of the particles, the nodes from SPH with the artificial stress have an isotropic configuration. The isotropy of the particles is an inherent feature of the artificial stress method, which acts to avoid voids in the material. It is this elimination of voids that inhibits the effects of the tensile instability. On the contrary, the particle positions in the SP2 method have formed structures that align with the trajectories of the soil movement. The presence of such structures is an indication of the accuracy of the scheme — the more accurate a meshless method is, the more likely that the particles will accurately follow the flow trajectories [63]. These results show that the Stress-Particle SPH method reduces the errors associated with the tensile instability without the need for any artificial stress.

Although anisotropic structures in SPH indicate the accuracy of the numerical technique, they may lead to subsequent deterioration of the simulation results. In standard SPH, such structures have been associated with a decrease in accuracy and stability of the model results — counteracting the benefits of the stabilising technique that caused the structures in the first place. The accuracy of the kernel approximation depends on the particle distribution, and can decline in areas where there is high particle disorder [62,64]. Oger et al. [63] showed for a range of fluid flow problems that the presence of anisotropic structures sometimes lead to particle disordering, which was detrimental to the performance of SPH. In the considered problems, the deterioration of the SPH simulation was mainly associated with noisy pressure fields. However, the Stress-Particle SPH method naturally smooths the pressure (or stress), thereby potentially resolving the problems that anisotropic particle structures can bring.

The results shown in Fig. 10 suggest that the presence of the anisotropic structures has not reduced the quality of the cohesive soil simulation. Nonetheless, it is beneficial to include a technique that can prevent the deterioration of the Stress-Particle method (due to anisotropic structures). One simple technique is to update the particle positions according to the XSPH method [65]:

$$\mathbf{x}_i^{t+\Delta t} = \mathbf{x}_i^t + \Delta t \left( \mathbf{u}_i^{t+\Delta t} + \epsilon_x \sum_{j=1}^N \frac{m_j}{\rho_j} (\mathbf{u}_j - \mathbf{u}_i) \nabla W_{ij} \right). \quad (38)$$

where  $\epsilon_x$  is a tuning parameter ( $0 \leq \epsilon_x \leq 1$ ). In the XSPH method, the position of each particle is updated with a velocity that is representative of the average velocity in its neighbourhood, rather than its individual velocity. Fig. 11 shows the particle positions at  $t = 2$  s for SP1 and SP2, updated with and without the XSPH method (with  $\epsilon_x = 0.5$ ). When the particle positions were not updated with XSPH, some particle disordering is present in both configurations in the upper half of the shear band. Conversely, when the XSPH method was used, the particles form smooth trajectories throughout the material for SP1 and SP2.

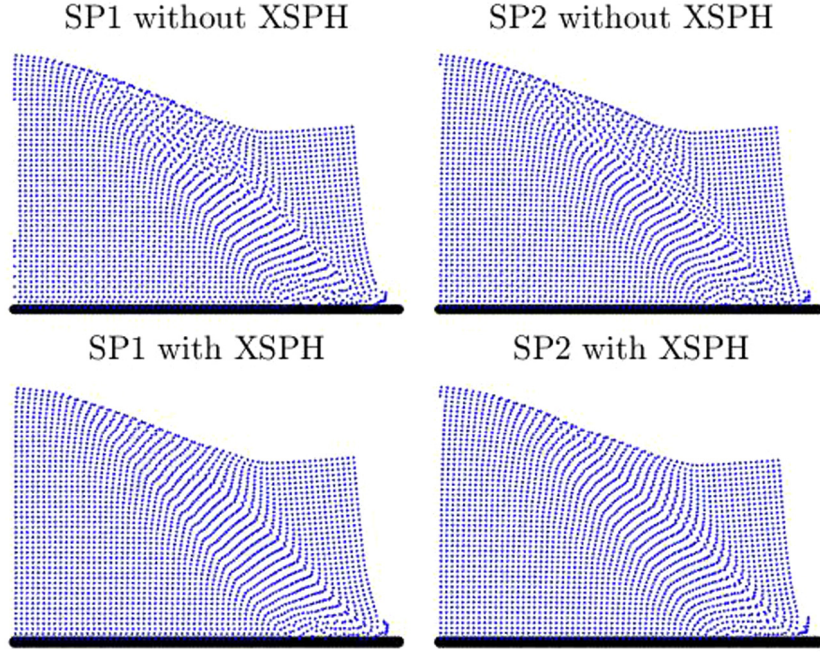


**Fig. 11.** The node positions at the front of the material at  $t = 2$  s, for the cohesive soil failure problem. The results show the effect of updating the node and stress-point positions with the XSPH method, for SP1 and SP2.

#### 4.3.2. Non-cohesive soil

The non-cohesive soil collapsed and propagated downstream at a rapid rate, exhibiting flow-type behaviour. Simulating this problem assesses how the Stress-Particle method can deal with high displacement problems that are relevant to the post-failure behaviour slopes.

The node and stress-point positions at  $t = 2.5$  s of the non-cohesive soil simulation are provided in Fig. 12 for configuration SP2. The nodes and stress-points are depicted by the circles and crosses respectively. It is evident that Stress-Particle SPH, with its current set-up, is unable to capture the dynamics of this problem. Similar results were also obtained for SP1 and SP3. The particles exhibit highly unstable behaviour at the front of the material — the stress-points are relatively sparse in this area for all configurations, which contributes to the deterioration of the simulation. The lack of stress-points at the material front is due to the fact that in high velocity problems, updating the position of the stress-points with an interpolated velocity does not ensure that there will always be a sufficient number of them in the support domain of each SPH node. Additionally, it is essential to include a repulsive boundary force that acts on the SPH nodes to prevent them from penetrating the boundary. This is also likely to interfere with the material behaviour, particularly when the material layer above the boundary is thin. Note that the particles in Fig. 12 were updated in the standard way, and the results were not improved when the nodes and stress-points were updated according to the XSPH method.

These results highlight the inability of the Stress-Particle SPH method in its current set-up at simulating problems with large displacements. In the following section, an improved Stress-Particle SPH model is presented, that enables the simulation of large displacement problems.

## 5. Stress-particle SPH: an improved model

The results presented in the previous section show that while Stress-Particle SPH is able to significantly reduce the detrimental effects of zero-energy modes and the tensile instability, it is unable to simulate problems involving large displacements and high velocities (one of the most appealing features of SPH) in its current framework. Therefore, we here present an extension of Stress-Particle SPH, to enable the simulation of large displacement problems. The extended model is applied to the large elastoplastic vertical slope problem described in the previous

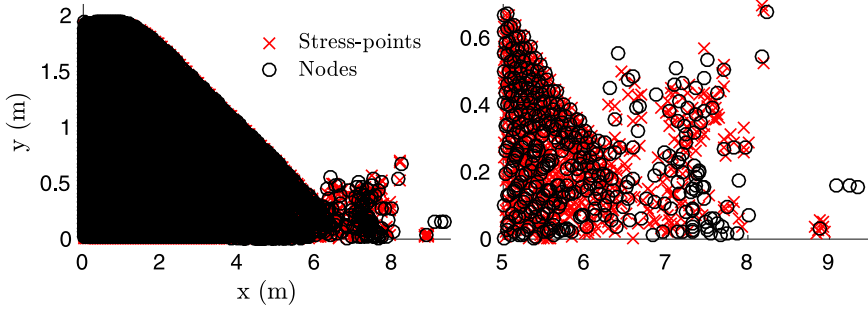


**Fig. 12.** Particle positions at  $t = 2.5$  s for the non-cohesive soil failure problem, calculated with the SP2 configuration.

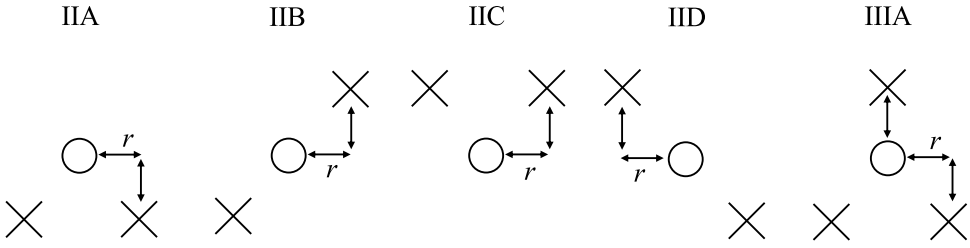


**Fig. 13.** A depiction of various node–stress-point configurations in the updated Stress-Particle SPH method.

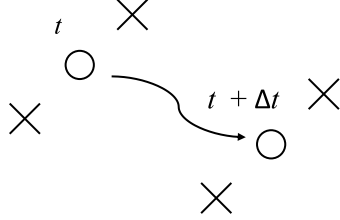


**Fig. 14.** A sketch depicting the stress-points positions following their associated node in the extended Stress-Particle method.

section. This problem exhibits all relevant features for the purpose of validating the abilities of Stress-Particle SPH (i.e. strain localisation, the tensile instability, zero-energy modes and large displacements).

Rather than having the stress-points initially placed inside virtual quadrilaterals, for the application to large displacements they are arranged with respect to each node — a predefined number of stress-points are assigned to every node, and associated with that node for the entire simulation. Examples of different configurations are provided in Fig. 13, where  $r$  specifies the vertical and horizontal distance of the stress-point from the node (in the current work we use  $r = \Delta x/3$ ). Other configurations were also explored from which we discovered that one stress-point per node is not adequate — probably because the effect of the stress point is weighted towards one side for the whole duration of the simulation. Arranging the stress-points as depicted in Fig. 13 offers a number of potential benefits for large displacement problems: as each node is associated with one or more stress-points, the stress-point positions can be updated according to the position of the node. The stress-points can therefore follow the node for the duration of the simulation (see Fig. 14), which ensures that there are always enough stress-points in the domain of influence of each node.

With the new method of updating the stress-point positions, it is no longer necessary to apply the boundary repulsive force that prevents the penetration of nodes through the boundaries. The positions of the stress-points that are in the neighbourhood of the wall boundary can be reassigned to be equal to that of their associated node (see Fig. 15). This essentially ‘turns off’ the stress-points in the wall proximity, and the method reduces to standard SPH (with extra variable smoothing according to (29) and (30)). Furthermore, recall that in the vertical cut problem there were disparities in the stress contours that were linked to the boundary–stress-point interactions (see Section 4.1).

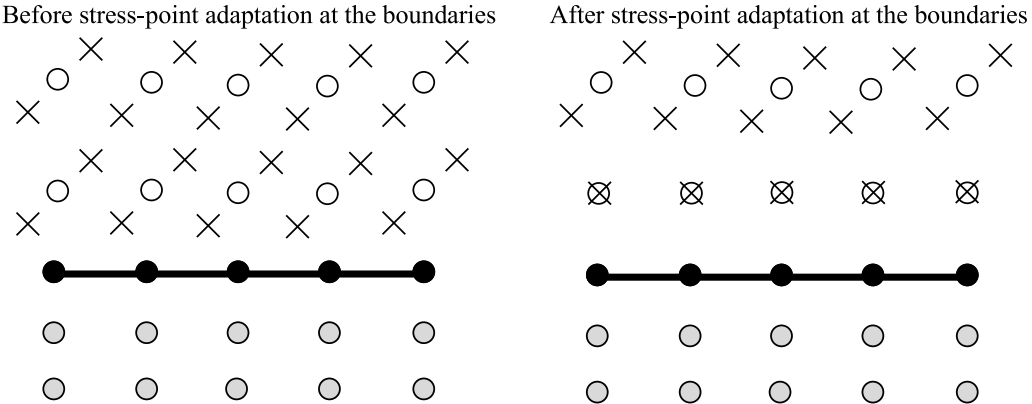


**Fig. 15.** A depiction of the nodes and stress-points in the updated Stress-Particle method, in the proximity of the wall boundary.

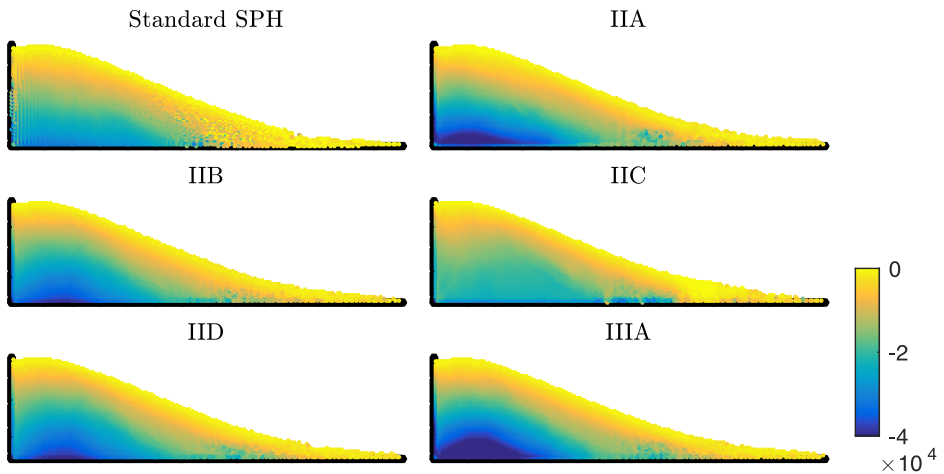


**Fig. 16.** Node positions at  $t = 2.5$  s for the non-cohesive soil failure problem coloured by vertical stress  $\sigma_{yy}$  (Pa), for alternative node–stress-point configurations (see Fig. 13). Note the noisy areas of the stress profile for the standard SPH results.

Removing the influence of the stress-points near the boundary eliminates the problems that were encountered in this area.

We have first applied the updated Stress-Particle SPH method to the non-cohesive soil problem. Fig. 16 displays the particle positions at  $t = 2.5$  with contours of vertical stress, for the different node–stress-point configurations. The XSPH method (with  $\epsilon_x = 0.5$ ) has been applied to update the node positions to prevent particle disordering, as discussed in Section 4.3.1. The Stress-Particle SPH results now exhibit the same behaviour as for standard SPH, and the large displacements have been captured well. Additionally, the stress profiles are significantly smoother overall than for standard SPH. However, note that the stress profiles differ somewhat between the alternative configurations.

In addition to being able to model flow-type problems, it is essential to verify whether Stress-Particle SPH with the new stress-point position update is still capable of removing the effects of the tensile instability. Therefore, we also apply the new model to the problem of the cohesive soil failure (described in Section 4.3.1). The deformed material at the end of the simulation is shown in Fig. 17, coloured by values of deviatoric plastic strain. The effects of the tensile instability have been reduced considerably in comparison to the standard SPH results (with no artificial stress, see Fig. 9). However, the new Stress-Particle method has not completely removed the effects of the instability for all of the node–stress-point configurations considered. Small fractures are present in the region of the soil under tension for both the IIB and IIIA configurations. The latter configuration consists of three stress-points per node, which shows that the performance of Stress-Particle SPH is not solely dependent on the quantity of the stress-points. Furthermore, the shape of the deformed material differs considerably between the different configurations.

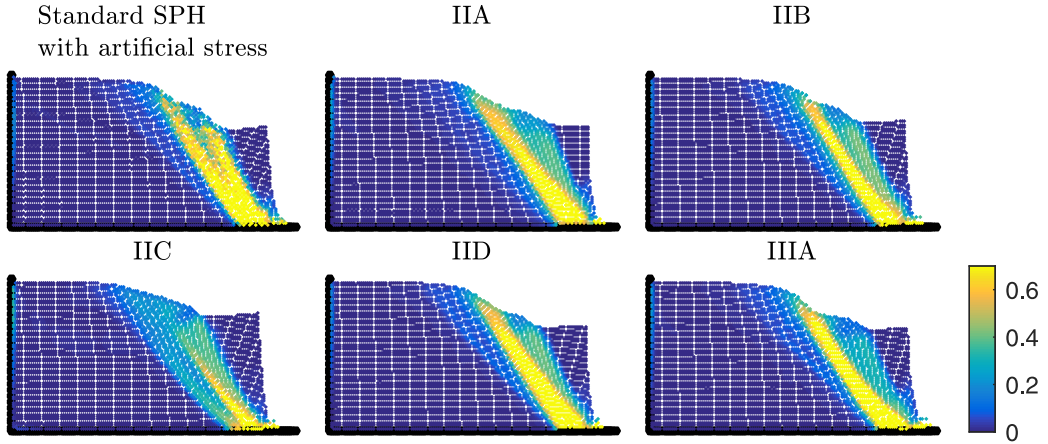


**Fig. 17.** The deformed material at  $t = 2.5$  s in the cohesive soil failure problem, coloured by values of deviatoric plastic strain  $\bar{\epsilon}^P$  (dimensionless). Displayed are the results computed with standard SPH and different configurations of the updated Stress-Particle method.

Differences of this magnitude were not observed between the SP1, SP2 and SP3 results, when the stress-points were updated according to their interpolated velocity. A description of how XSPH affects the particle trajectories when the stress-points are updated with the new method is provided in [Appendix F](#).

It is important to highlight that of the results displayed in [Fig. 17](#), those produced with configuration IID bear the closest resemblance to the standard SPH profile (with the artificial stress). Configuration IID consists of two stress-points positioned diagonally around each node, as depicted in [Fig. 13](#). This configuration aligns most closely with the direction of the flow in the cohesive soil failure. When the stress-points are updated according to their interpolated velocities, they naturally align with the overall motion of the flow (for relatively low displacement problems). Therefore, we deduce that the stress-points should be aligned in the general flow direction in order to combat the tensile instability and produce accurate free surface profiles. It is reasonable to conclude that it is unnatural to have stress-points positioned in areas where there would not usually be a material point to influence the stress calculations on a node.

### 5.1. Further developments: the velocity vector approach

An alternative way in which to update the stress-point positions is to consider the velocity vector at each node throughout the simulation. In this method – named the *velocity vector approach* – the stress-points follow their associated node throughout the simulation (thereby allowing the simulation of large displacements), yet their orientation is adapted to align with the velocity vector of that node. A description of the method is given as follows. The stress-points are initially positioned with respect to each node in a specified configuration. At each time step, the components of the velocity are utilised to calculate the angle of direction of the velocity vector  $\theta_u$ :

$$\cos \theta_u = u_x / |\mathbf{u}|, \quad \sin \theta_u = u_y / |\mathbf{u}|. \quad (39)$$

The horizontal and vertical components of the position vector of each stress-point, denoted by  $r_x$  and  $r_y$  respectively, are calculated as

$$r_x = r \cos \theta_u, \quad r_y = r \sin \theta_u, \quad (40)$$

where now  $r$  is the specified total distance of each stress-point to the node. As before, we select  $r = \Delta x / 3$ . At each node with position vector  $(x_i, y_i)$ , two stress-points are placed with the position vectors  $(x_i + r_x, y_i + r_y)$  and  $(x_i - r_x, y_i - r_y)$ , as depicted in [Fig. 18](#). This ensures that each node is associated with two stress-points that are both aligned with the velocity vector of that node. Additionally, the stress-point distribution at each node is symmetric with respect to the normal velocity, and the influence of the stress-point is not weighted towards one side.

An area where the velocity vector method may break down is when the velocity is dominant in either the vertical or horizontal direction. For example, if the horizontal velocity is negligible, the angle  $\theta_u$  is approximately zero and

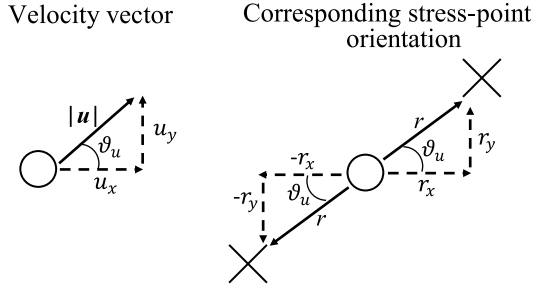


**Fig. 18.** A depiction of the velocity vector at an individual node, and the corresponding stress-point placement.

the stress-points will be aligned with the nodes in vertical structures. In general, a staggered node–stress-point arrangement is preferable [27]. Therefore, the method is adapted so that the horizontal and vertical distances are increased if they are below a threshold value. We assume a sufficient threshold to be  $\Delta x/5$ , which is implemented as follows.

$$\text{if } |r_x| < \Delta x/5, \quad |r_x| = |r_x| + \Delta x/3, \quad (41)$$

$$\text{if } |r_y| < \Delta x/5, \quad |r_y| = |r_y| + \Delta x/3. \quad (42)$$

Applying Eqs. (41) and (42) still ensures that the stress-points are orientated in the direction of the node velocities — they are simply shifted horizontally or vertically to also allow a staggered node–stress-point arrangement.

Another factor to consider in the velocity vector approach is small scale node fluctuations (which are often inevitable in meshless methods). Such fluctuations would result in rapid changes in stress-point orientation — as the method is independent of velocity magnitude, the stress-point placement is identical for two nodes travelling in the same direction at different speeds. To account for small scale fluctuations, we only update the stress-point positions of the nodes that have moved more than a specified distance, over a specified time period. If the relative displacement of a node is greater than the threshold value over the considered time, we shift the stress-points according to (40). Otherwise, we do not adapt the stress-point positions. In the current work, we found an acceptable displacement tolerance to be  $0.125\Delta x$ , over a time period of 1000 time steps. Some trial and error was required to obtain these values — future work should incorporate a more universal solution to remove the effects of small scale node fluctuations.

Contour plots of deviatoric plastic strain and stress are provided in Fig. 19 for the cohesive and non-cohesive soil problems respectively, where the stress-points were defined to align with the node velocity vectors as described above. In both cases, it can be seen that variable profiles are smooth throughout, and the expected material behaviour has been captured well. The effects of the tensile instability have been removed completely in the cohesive soil, and the large displacements of the non-cohesive soil have been simulated with accuracy. XSPH was included to update the node positions for the results shown in Fig. 19. Although the use of XSPH is not essential for stable and accurate results, it prevents particle disordering (see Appendix F).

## 6. Conclusions

We have implemented stress-points within SPH with the purpose of removing the two most detrimental instabilities from the meshless method — zero-energy modes, and the tensile instability. The adapted SPH model – Stress-Particle SPH – has been applied to problems that are relevant to the failure and post-failure behaviour of slopes. This is the first time that SPH with stress-points has been used to simulate problems involving soil dynamics and slope failure. We have shown that Stress-Particle SPH is capable of eliminating or considerably reducing the effects of both instabilities. Most significantly, it is able to eliminate the severe fracturing due to the tensile instability in a cohesive soil. Additionally, Stress-Particle SPH remedies the instabilities without the need for artificial tuning parameters.

The most significant contribution of the current work is the adaptation and extension of Stress-Particle SPH for applicability to large displacement problems. We have developed a novel way in which to update the stress-points positions that ensures there are always enough stress-points in the vicinity of each node. Moreover, we have shown

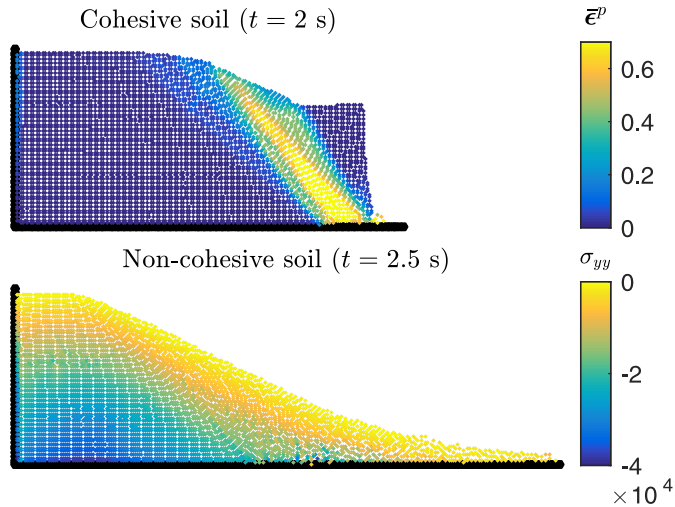


**Fig. 19.** The final node positions for the cohesive and non-cohesive soil problems, coloured by deviatoric plastic strain  $\bar{\epsilon}^p$  (dimensionless) and vertical stress  $\sigma_{yy}$  (Pa) respectively. The stress-point positions were updated to align with the velocity vector at each node, according to the velocity vector method.

that the orientation of the stress-points is in fact more significant than their quantity. The stress-points should be aligned with the general flow direction to produce accurate results — we have extended the Stress-Particle SPH method accordingly. The resulting extension — the velocity vector approach — is able to capture large displacements (relevant to post-failure slope behaviour), as well as stabilise the system. This is the first time that stress-points have been implemented in a meshless method and used to simulate problems with large displacements and high velocities.

Some further developments are required to optimise the novel Stress-Particle SPH method. First, the computational expense is significantly higher than that of standard SPH. For example, the simulation of the cohesive soil failure with SP1 takes approximately double the length of time than for standard SPH (with one computational processing unit). With an increase in the node–stress-point ratio, the computational time increases by a factor of approximately 1.6. Techniques such as parallel computing and the implementation of graphics processing units could be utilised to improve the efficiency of Stress-Particle SPH. Furthermore, in the final, extended version of the method presented in Section 5, some trial and error is required to remove the effects of the small scale node oscillations. Future work may involve a more sophisticated method for this, perhaps by considering the velocity magnitude in addition to the direction. Despite these factors, the developments to Stress-Particle SPH presented here offer the potential for SPH to simulate a broader range of problems than it is capable of in its standard form. Further simulations of different problems are required in order to fully test the capabilities of Stress-Particle SPH, including applications beyond slope behaviour.

### Declaration of competing interest

The authors declare that they have no known competing financial interests or personal relationships that could have appeared to influence the work reported in this paper.

### Acknowledgements

This work was supported by the Engineering and Physical Sciences Research Council (EPSRC) United Kingdom Centre for Doctoral Training in Fluid Dynamics at the University of Leeds under Grant No. EP/L01615X/1. We thank the two anonymous reviewers for their helpful feedback and suggestions. Professor Manuel Pastor would like to thank the Ministry of Economy and Competitiveness (MINECO) Spain for their role in supporting this research.

## Appendix A. Constitutive model

Here we provide further detail on the derivation of the constitutive model presented briefly in Section 2. The fundamental assumption is the division of the total strain rate into an elastic and plastic component, where the latter is responsible for all irreversible deformations. We define the elastic strains according to the generalised Hooke's law:

$$\dot{\epsilon}_e = \frac{\dot{s}}{2G} + \frac{1-2\nu}{3E} \dot{\sigma}_{kk} \mathbf{I}. \quad (\text{A.1})$$

Here,  $\dot{\sigma}_{kk} = \dot{\sigma}_{xx} + \dot{\sigma}_{yy} + \dot{\sigma}_{zz}$ ,  $s$  is the deviatoric stress tensor:  $s = \sigma - p\mathbf{I}$ , where  $p = \sigma_{kk}/3$  is hydrostatic pressure and  $\mathbf{I}$  is the identity matrix. We also define the total strain rate via the kinematic condition, which relates the total deformation to the velocity gradients:

$$\dot{\epsilon}_{ij} = \frac{1}{2} \left( \frac{\partial u_i}{\partial x_j} + \frac{\partial u_j}{\partial x_i} \right), \quad (\text{A.2})$$

where  $i$  and  $j$  denote the  $x$ ,  $y$  and  $z$  components in Cartesian coordinates. The definition of the plastic strain rate depends on the choice of constitutive model — we consider both an elastoplastic model (derived from classic plasticity), and a viscoplastic Perzyna model. In both cases, elastic and plastic behaviour are distinguished via a stress-dependent yield criterion.

### A.1. Yield criteria

The yield function  $f$  is typically defined in terms of the stress invariants. Here we define the first invariant of the stress tensor  $I_1$ , and the second invariant of the deviatoric stress tensor  $J_2$ :

$$I_1 = \sigma_{xx} + \sigma_{yy} + \sigma_{zz}, \quad J_2 = \frac{1}{2} s : s. \quad (\text{A.3})$$

The yield criteria of interest in the current work are those of Von Mises and Drucker–Prager. The Von Mises criterion is a function of the second invariant of the deviatoric tensor:

$$f = \sqrt{3J_2} - f_c, \quad (\text{A.4})$$

where  $f_c$  is a constant stress value. The criterion has the benefit of being simple, but is only relevant when modelling soils of a clay-type. It does not take the hydrostatic pressure of the material into account, which has been shown to play a role in the strength of granular materials [66]. The Drucker–Prager criterion – an adapted version of Mohr–Coulomb – does include hydrostatic stress dependence. It is defined in terms of the second deviatoric stress invariant and the first invariant of the stress tensor:

$$f = \sqrt{J_2} + \alpha_\phi I_1 - k_c = 0, \quad (\text{A.5})$$

where  $\alpha_\phi$  and  $k_c$  are model parameters. These are functions of the Coulomb material constants — the soil internal friction  $\phi$  and cohesion  $c_{oh}$ :

$$\alpha_\phi = \frac{\tan \phi}{\sqrt{9 + 12 \tan^2 \phi}} \quad \text{and} \quad k_c = \frac{3c_{oh}}{\sqrt{9 + 12 \tan^2 \phi}}. \quad (\text{A.6})$$

The Von Mises and Drucker–Prager yield criteria are illustrated in two dimensions in Fig. 20. In each case, when the stress state does not lie within the elastic region, the material exhibits plastic strains. Note that once plastic strains have occurred, the size of the yield surface may vary according to a suitable hardening or softening law. Otherwise, the material is perfectly plastic.

### A.2. Elastoplastic model

In the derivation of the elastoplastic model, the plastic strain rate is defined via the plastic flow rule:

$$\dot{\epsilon}^p = \lambda \frac{\partial g}{\partial s}, \quad (\text{A.7})$$

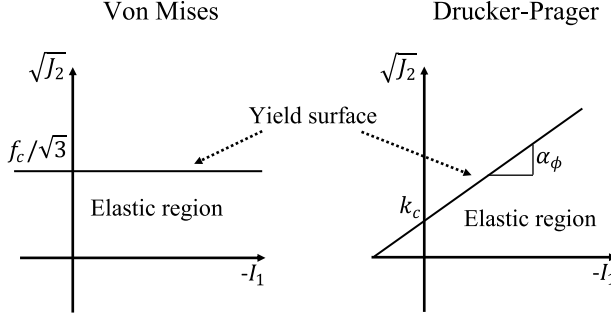


Fig. 20. Yield criteria in the  $(-I_1, \sqrt{J_2})$  plane.

where  $\dot{\lambda}$  is the consistency parameter and  $g$  is the plastic potential function. Along with the elastic strain rate (A.1), (A.7) is substituted into the equation for the total strain rate (3). The deviatoric stress tensor is then rewritten in terms of the total stress to obtain a stress–strain relationship:

$$\frac{D\sigma}{Dt} = 2G\dot{\epsilon} + K\dot{\epsilon}_{kk}\mathbf{I} - \dot{\lambda} \left( \left( K - \frac{2G}{3} \right) \left( \frac{\partial g}{\partial \sigma} : \mathbf{I} \right) \mathbf{I} + 2G \frac{\partial g}{\partial \sigma} \right). \quad (\text{A.8})$$

Here,  $\dot{\epsilon} = \dot{\epsilon} - (\dot{\epsilon}_{kk}/3)\mathbf{I}$  is the deviatoric strain rate tensor,  $G = E/2(1+\nu)$  is the shear modulus and  $K = E/3(1-2\nu)$  is the elastic bulk modulus. The first two terms on the right hand side of (A.8) describe the elastic deformations, while the latter describes the plastic.

Under the theory of classic plasticity, the plastic multiplier  $\lambda$  must satisfy the following criteria:

$$\lambda = \begin{cases} 0, & \text{if } f < 0, \\ 0, & \text{if } f = 0 \text{ and } df < 0 \\ \lambda > 0, & \text{if } f = 0 \text{ and } df = 0, \end{cases} \quad (\text{A.9})$$

where  $df$  is the increment of the yield function after plastic loading or unloading. The stress state is not allowed to exceed the yield surface, and the yield function increment cannot be greater than zero. Plastic loading is characterised by a non-zero value of the plastic multiplier  $\lambda$ , calculated according to the consistency condition:

$$df = \frac{\partial f}{\partial \sigma} d\sigma = 0, \quad (\text{A.10})$$

which ensures that the stress state remains on the yield surface during plastic loading. Eq. (A.8) is substituted into the consistency condition (A.10), and rearranged to obtain  $\dot{\lambda}$ :

$$\dot{\lambda} = \frac{2G\dot{\epsilon} : \frac{\partial f}{\partial \sigma} + \dot{\epsilon}_{kk} \left( K - \frac{2G}{3} \right) \left( \frac{\partial f}{\partial \sigma} : \mathbf{I} \right)}{2G \left( \frac{\partial f}{\partial \sigma} : \frac{\partial g}{\partial \sigma} \right) + \left( K - \frac{2G}{3} \right) \left( \frac{\partial f}{\partial \sigma} : \mathbf{I} \right) \left( \frac{\partial g}{\partial \sigma} : \mathbf{I} \right)}. \quad (\text{A.11})$$

Eq. (A.11) is closed upon substitution of  $f$  and  $g$ . Following Bui et al. [20], we implement a Drucker–Prager yield criterion, with a non-associated flow rule ( $f \neq g$ ). The plastic potential function is defined as

$$g = \sqrt{J_2} + 3I_1 \sin \psi, \quad (\text{A.12})$$

where  $\psi$  is the dilatancy angle, which we assume to be zero. After the substitution of (A.12) and the Drucker–Prager yield function (A.5), the elastoplastic constitutive equation is

$$\frac{D\sigma}{Dt} = 2G\dot{\epsilon} + K\dot{\epsilon}_{kk}\mathbf{I} - \dot{\lambda} \left( 9K \sin \psi \mathbf{I} + \frac{G}{\sqrt{J_2}} \mathbf{s} \right), \quad (\text{A.13})$$

where

$$\dot{\lambda} = \frac{3\alpha_\phi \dot{\epsilon}_{kk} + (G/\sqrt{J_2}) \mathbf{s} : \dot{\epsilon}}{27\alpha_\phi K \sin \psi + G}. \quad (\text{A.14})$$

For a dilatancy angle of zero, (A.13) and (A.14) reduce to

$$\frac{D\sigma}{Dt} = 2G\dot{\epsilon} + K\dot{\epsilon}_{kk}\mathbf{I} - \lambda \frac{G}{\sqrt{J_2}s}, \quad (\text{A.15})$$

$$\dot{\lambda} = \frac{3\alpha_\phi\dot{\epsilon}_{kk} + (G/\sqrt{J_2})s : \dot{\epsilon}}{G}. \quad (\text{A.16})$$

A detailed description of the elastoplastic constitutive model can be found in references [3] and [20].

### A.3. Perzyna model

The viscoplastic Perzyna model was developed as an alternative to the classic elastoplastic model, motivated by the fact that many solid materials exhibit viscous effects [46]. An alternative definition of Hooke's law is considered in the derivation of the Perzyna model:

$$\frac{D\sigma}{Dt} = \mathbf{D}^e : \dot{\epsilon}^e, \quad (\text{A.17})$$

where  $\mathbf{D}^e$  is the elastic constitutive matrix, which is a fourth-order tensor consisting of 81 material constants in three dimensions. Note that (A.17) is equivalent to (A.1) for an isotropic material. The elastic strain rate is then rearranged in terms of the total and plastic strain rate:

$$\frac{D\sigma}{Dt} = \mathbf{D}^e : (\dot{\epsilon} - \dot{\epsilon}^p), \quad (\text{A.18})$$

In the Perzyna model, the plastic strain rate is defined as

$$\dot{\epsilon}^p = \frac{\partial g}{\partial \sigma} \gamma \langle \phi(F) \rangle, \quad (\text{A.19})$$

where  $\gamma$  is a fluidity parameter (which acts as the reciprocal of viscosity) and  $\phi(F)$  is a yield-type function. The (...) symbol represents the Macaulay brackets:

$$\langle \phi \rangle = \begin{cases} \phi, & \phi \geq 0 \\ 0, & \phi < 0, \end{cases}$$

and the function  $\phi(F)$  is therefore defined as

$$\phi(F) = \left( \frac{F - F_0}{F_0} \right)^{\hat{N}}. \quad (\text{A.20})$$

Here,  $\hat{N}$  is a model parameter,  $F$  is a function of the stress state (related to the yield function), and  $F_0$  defines a critical stress value for plastic strains. Plastic strains are non-zero when the function  $F$  exceeds the critical value  $F_0$ , such that

$$\langle \phi(F) \rangle = \begin{cases} \phi(F), & \text{if } F > F_0 \\ 0, & \text{if } F \leq F_0. \end{cases} \quad (\text{A.21})$$

Note that unlike the elastoplastic constitutive model, the Perzyna model permits the stress state to exceed the yield surface. Following Blanc [29] and Blanc and Pastor [31], we consider a Von Mises yield function within the Perzyna model, with an associated flow rule ( $f = g$ ). In terms of  $F$  and  $F_0$ , the Von Mises yield criterion is defined as

$$F = \sqrt{3J_2} \quad \text{and} \quad F_0 = f_c. \quad (\text{A.22})$$

Plastic flow therefore occurs when  $\sqrt{3J_2} > f_c$ , where  $f_c$  is a critical stress value that may vary according to a hardening or softening law. With Eq. (A.22) and  $g = \sqrt{3J_2} - f_c$ , the Perzyna model is written as:

$$\frac{D\sigma}{Dt} = \mathbf{D}^e : \dot{\epsilon} - \mathbf{D}^e : \frac{\partial \sqrt{3J_2}}{\partial \sigma} \left( \frac{\sqrt{3J_2} - f_c}{f_c} \right)^{\hat{N}}. \quad (\text{A.23})$$

Further details on the derivation of the Perzyna model can be found in reference [29].

#### A.4. A general constitutive model in plane strain

The analysis in the current work is restricted to problems in plane strain, where the velocity, stress and strain rate are defined as the following vectors:

$$\mathbf{u} = \begin{pmatrix} u_x \\ u_y \end{pmatrix}, \quad \boldsymbol{\sigma} = \begin{pmatrix} \sigma_{xx} \\ \sigma_{yy} \\ \sigma_{xy} \\ \sigma_{zz} \end{pmatrix}, \quad \dot{\boldsymbol{\epsilon}} = \begin{pmatrix} \dot{\epsilon}_{xx} \\ \dot{\epsilon}_{yy} \\ 2\dot{\epsilon}_{xy} \\ 0 \end{pmatrix}. \quad (\text{A.24})$$

Furthermore, in plane strain the elastic constitutive matrix reduces to a  $4 \times 4$  matrix:

$$\mathbf{D}^e = \frac{E}{(1+v)(1-2v)} \begin{pmatrix} 1-v & v & 0 & v \\ v & 1-v & 0 & v \\ 0 & 0 & (1-2v)/2 & 0 \\ v & v & 0 & 1-v \end{pmatrix}. \quad (\text{A.25})$$

Regarding the Perzyna constitutive model, it can now be written in plane strain as

$$\frac{D\sigma}{Dt} = \mathbf{D}^e \dot{\boldsymbol{\epsilon}} - \mathbf{D}^e \frac{\partial \sqrt{3J_2}}{\partial \sigma} \left( \frac{\sqrt{3J_2} - f_c}{f_c} \right)^{\hat{N}}, \quad (\text{A.26})$$

where

$$\mathbf{D}^e \dot{\boldsymbol{\epsilon}} = \begin{pmatrix} D_{11}\dot{\epsilon}_{xx} + D_{12}\dot{\epsilon}_{yy} \\ D_{21}\dot{\epsilon}_{xx} + D_{22}\dot{\epsilon}_{yy} \\ D_{33}2\dot{\epsilon}_{xy} \\ D_{41}\dot{\epsilon}_{xx} + D_{42}\dot{\epsilon}_{yy} \end{pmatrix}. \quad (\text{A.27})$$

Note that  $D_{11} = D_{22} = D_{44}$ , and  $D_{12} = D_{21} = D_{41} = D_{42}$ . The elastoplastic constitutive model requires further manipulation to clearly show how it can be written in a compact form in plane strain. For this, it is convenient to write the full constitutive equation in tensor notation:

$$\frac{D\sigma_{ij}}{Dt} = 2G\dot{e}_{ij} + K\dot{\epsilon}_{kk}\delta_{ij} - \dot{\lambda} \frac{G}{\sqrt{J_2}s_{ij}}, \quad (\text{A.28})$$

where  $\delta_{ij}$  is the kronecker delta. In plane strain, the plastic term is written as

$$\dot{\lambda} \frac{G}{\sqrt{J_2}s}, \quad (\text{A.29})$$

where we now define  $\mathbf{s}$  as a vector:

$$\mathbf{s} = \begin{pmatrix} s_{xx} \\ s_{yy} \\ s_{xy} \\ s_{zz} \end{pmatrix} = \begin{pmatrix} \sigma_{xx} - (\sigma_{xx} + \sigma_{yy})/3 \\ \sigma_{yy} - (\sigma_{xx} + \sigma_{yy})/3 \\ \sigma_{xy} \\ -(\sigma_{xx} + \sigma_{yy})/3 \end{pmatrix}. \quad (\text{A.30})$$

Next, we consider the terms responsible for elastic deformations:

$$2G\dot{e}_{ij} + K\dot{\epsilon}_{kk}\delta_{ij} = 2G(\dot{\epsilon}_{ij} - \delta_{ij}\dot{\epsilon}_{kk}/3) + K\dot{\epsilon}_{kk}\delta_{ij}. \quad (\text{A.31})$$

First, consider the case when  $i = j = x$ :

$$2G\dot{\epsilon}_{xx} + K\dot{\epsilon}_{kk} = 2G\dot{\epsilon}_{xx} + \left(K - \frac{2G}{3}\right)\dot{\epsilon}_{kk} \quad (\text{A.32})$$

$$= 2G\dot{\epsilon}_{xx} + \left(K - \frac{2G}{3}\right)(\dot{\epsilon}_{xx} + \dot{\epsilon}_{yy}) \quad (\text{A.33})$$

$$= \left(2G + K - \frac{2G}{3}\right)\dot{\epsilon}_{xx} + \left(K - \frac{2G}{3}\right)\dot{\epsilon}_{yy} \quad (\text{A.34})$$

$$= \left(\frac{E}{1+\nu} + \frac{E}{3(1-2\nu)} - \frac{E}{3(1+\nu)}\right)\dot{\epsilon}_{xx} + \left(\frac{E}{3(1-2\nu)} - \frac{E}{3(1+\nu)}\right)\dot{\epsilon}_{yy} \quad (\text{A.35})$$

$$= \left(\frac{E(1-\nu)}{(1-2\nu)(1+\nu)}\right)\dot{\epsilon}_{xx} + \frac{Ev}{(1-2\nu)(1+\nu)}(\dot{\epsilon}_{yy}) \quad (\text{A.36})$$

$$= D_{11}\dot{\epsilon}_{xx} + D_{12}\dot{\epsilon}_{yy}. \quad (\text{A.37})$$

Similarly, for  $i = j = y$ :

$$2G\dot{\epsilon}_{yy} + K\dot{\epsilon}_{kk} = \left(2G + K - \frac{2G}{3}\right)\dot{\epsilon}_{yy} + \left(K - \frac{2G}{3}\right)\dot{\epsilon}_{xx} \quad (\text{A.38})$$

$$= \left(\frac{E(1-\nu)}{(1-2\nu)(1+\nu)}\right)\dot{\epsilon}_{yy} + \frac{Ev}{(1-2\nu)(1+\nu)}(\dot{\epsilon}_{xx}) \quad (\text{A.39})$$

$$= D_{21}\dot{\epsilon}_{xx} + D_{22}\dot{\epsilon}_{yy}. \quad (\text{A.40})$$

When  $i = x, j = y$  (or vice versa):

$$2G\dot{\epsilon}_{xy} = 2G\dot{\epsilon}_{xy} \quad (\text{A.41})$$

$$= \left(\frac{E}{1+\nu}\right)\dot{\epsilon}_{xy} \quad (\text{A.42})$$

$$= 2D_{33}\dot{\epsilon}_{xy}. \quad (\text{A.43})$$

Finally, for  $i = j = z$ :

$$2G\dot{\epsilon}_{zz} + K\dot{\epsilon}_{kk} = \left(K - \frac{2G}{3}\right)\dot{\epsilon}_{yy} + \left(K - \frac{2G}{3}\right)\dot{\epsilon}_{xx} \quad (\text{A.44})$$

$$= \left(\frac{Ev}{(1-2\nu)(1+\nu)}\right)\dot{\epsilon}_{yy} + \frac{Ev}{(1-2\nu)(1+\nu)}(\dot{\epsilon}_{xx}) \quad (\text{A.45})$$

$$= D_{41}\dot{\epsilon}_{xx} + D_{42}\dot{\epsilon}_{yy}. \quad (\text{A.46})$$

In plane strain, all other components are zero. Thus, we see that the elastic terms in the elastoplastic constitutive model in plane strain are equivalent to those in the viscoplastic Perzyna model. We now write the elastoplastic model as

$$\frac{D\sigma}{Dt} = \mathbf{D}^e\dot{\boldsymbol{\epsilon}} - \lambda \frac{G}{\sqrt{J_2}}\mathbf{s}\dot{\boldsymbol{\epsilon}}_{ij}, \quad (\text{A.47})$$

with

$$\dot{\lambda} = \frac{3\alpha_\phi\dot{\epsilon}_{kk} + (G/\sqrt{J_2})\mathbf{s}\dot{\boldsymbol{\epsilon}}_{ij}}{G}. \quad (\text{A.48})$$

where  $\dot{\boldsymbol{\epsilon}}$  is the vector defined in (A.24).

It is now evident that the only differences between the elastoplastic and Perzyna constitutive models lie within the terms responsible for plastic deformations. In both models, the plastic terms are functions of the plastic strain rate, which is dependent on the state of stress and material parameters. We therefore write the two models in a single, general form as

$$\frac{D\sigma}{Dt} = \mathbf{D}^e\dot{\boldsymbol{\epsilon}} - \mathbf{g}^{e_p}, \quad (\text{A.49})$$

where  $\mathbf{g}^{\epsilon^p}$  is a vector containing the plastic terms:

$$\mathbf{g}^{\epsilon^p} = \begin{pmatrix} g_{xx}^{\epsilon^p}(\dot{\epsilon}^p) \\ g_{yy}^{\epsilon^p}(\dot{\epsilon}^p) \\ g_{xy}^{\epsilon^p}(\dot{\epsilon}^p) \\ g_{zz}^{\epsilon^p}(\dot{\epsilon}^p) \end{pmatrix}. \quad (\text{A.50})$$

For the elastoplastic model,

$$\mathbf{g}^{\epsilon^p} = \dot{\lambda} \frac{G}{\sqrt{J_2 s}}, \quad (\text{A.51})$$

which is non-zero only when  $f = \sqrt{J_2} + \alpha_\phi I_1 - k_c = 0$  (and  $df = 0$ ), according to the Drucker–Prager yield criterion. For the Perzyna model,

$$\mathbf{g}^{\epsilon^p} = \mathbf{D}^e \frac{\partial \sqrt{3J_2}}{\partial \sigma} \left( \frac{\sqrt{3J_2} - f_c}{f_c} \right)^{\hat{N}}, \quad (\text{A.52})$$

which is non-zero only when  $\sqrt{3J_2} > f_c$  (according to the Von Mises yield criteron).

For the SPH discretisation it is convenient to write the elastic term in (A.49) as a function of the velocity gradients. Substituting (A.2) into (A.27), we get

$$\mathbf{D}^e \dot{\epsilon} = \frac{\partial}{\partial x} \begin{pmatrix} D_{11}^e u_x \\ D_{12}^e u_x \\ D_{33}^e u_y \\ D_{41}^e u_x \end{pmatrix} + \frac{\partial}{\partial y} \begin{pmatrix} D_{12}^e u_y \\ D_{22}^e u_y \\ D_{33}^e u_x \\ D_{42}^e u_y \end{pmatrix}. \quad (\text{A.53})$$

We then introduce the matrix  $\mathbf{f}^u$ :

$$\mathbf{f}^u = \begin{pmatrix} D_{11}^e u_x & D_{12}^e u_y \\ D_{12}^e u_x & D_{22}^e u_y \\ D_{33}^e u_y & D_{33}^e u_x \\ D_{41}^e u_x & D_{42}^e u_y \end{pmatrix}, \quad (\text{A.54})$$

and define the general, compact constitutive equation as

$$\frac{D\sigma}{Dt} = \nabla \cdot \mathbf{f}^u - \mathbf{g}^{\epsilon^p}. \quad (\text{A.55})$$

## Appendix B. RK4 time integration

We have utilised a fourth order Runge–Kutta (RK4) scheme to update the governing soil equations in time. Consider a general ordinary differential equation for a variable  $\phi$  with an initial condition  $\phi^0$  at an initial time  $t^0$ :

$$\dot{\phi} = f(t, \phi), \quad \phi(t^0) = \phi^0,$$

where  $f$  is a function of  $\phi$  and time  $t$ . The RK4 method is employed to increment  $\phi$  by a time step  $\Delta t$  to obtain the solution at time  $t = t + \Delta t$ :

$$\phi^{t+\Delta t} = \phi^t + \frac{\Delta t}{6}(k_1 + 2k_2 + 2k_3 + k_4). \quad (\text{B.1})$$

$$k_1 = f(\phi_1), \quad k_2 = f(\phi_2), \quad k_3 = f(\phi_3), \quad k_4 = f(\phi_4), \quad (\text{B.2})$$

$$\phi_1 = \phi^t, \quad \phi_2 = \phi^t + \frac{\Delta t}{2}k_1, \quad \phi_3 = \phi^t + \frac{\Delta t}{2}k_2, \quad \phi_4 = \phi^t + \Delta t k_3. \quad (\text{B.3})$$

Here, we describe the RK4 method with respect to the discrete standard SPH equations:

$$\frac{D\mathbf{u}_i}{Dt} = \sum_{j=1}^N m_j \left( \frac{\mathbf{f}_i^\sigma}{\rho_i^2} + \frac{\mathbf{f}_j^\sigma}{\rho_j^2} \right) \cdot \nabla W_{ij} + \mathbf{b}_i, \quad (\text{B.4})$$

$$\frac{D\sigma_i}{Dt} = \tilde{\sigma}_i + \sum_{j=1}^N \frac{m_j}{\rho_j} (\mathbf{f}_j^\sigma - \mathbf{f}_i^\sigma) \cdot \nabla W_{ij} - \mathbf{g}_i^{\epsilon^p}, \quad (\text{B.5})$$

where  $\mathbf{f}^\sigma = \mathbf{f}^\sigma(\sigma)$  and  $\mathbf{f}^u = \mathbf{f}^u(u)$  are functions of stress and velocity respectively. It is convenient to write (B.4) and (B.5) as

$$\frac{Du_i}{Dt} = F_1(\sigma), \quad (\text{B.6})$$

$$\frac{D\sigma_i}{Dt} = F_2(u, \sigma), \quad (\text{B.7})$$

where

$$F_1(\sigma) = \sum_{j=1}^N m_j \left( \frac{\mathbf{f}_i^\sigma}{\rho_i^2} + \frac{\mathbf{f}_j^\sigma}{\rho_j^2} \right) \cdot \nabla W_{ij} + \mathbf{b}_i \quad (\text{B.8})$$

$$F_2(u, \sigma) = \tilde{\sigma}_i + \sum_{j=1}^N \frac{m_j}{\rho_j} (\mathbf{f}_j^u - \mathbf{f}_i^u) \cdot \nabla W_{ij} - \mathbf{g}_i^{\epsilon^p}. \quad (\text{B.9})$$

Note that  $F_2$  is a function of both stress and velocity. Using the RK4 method, (B.6) and (B.7) are incremented in time at each SPH node as

$$u_i^{t+\Delta t} = u_i^t + \frac{\Delta t}{6} (F_1(\sigma_1) + 2F_1(\sigma_2) + 2F_1(\sigma_3) + F_1(\sigma_4)), \quad (\text{B.10})$$

$$\sigma_i^{t+\Delta t} = \sigma_i^t + \frac{\Delta t}{6} (F_2(u_1, \sigma_1) + 2F_2(u_2, \sigma_2) + 2F_2(u_3, \sigma_3) + F_2(u_4, \sigma_4)), \quad (\text{B.11})$$

where

$$u_1 = u^t \quad \sigma_1 = \sigma^t \quad (\text{B.12})$$

$$u_2 = u^t + \frac{\Delta t}{2} (F_1(\sigma_1)) \quad \sigma_2 = \sigma^t + \frac{\Delta t}{2} (F_2(u_1, \sigma_1)) \quad (\text{B.13})$$

$$u_3 = u^t + \frac{\Delta t}{2} (F_1(\sigma_2)) \quad \sigma_3 = \sigma^t + \frac{\Delta t}{2} (F_2(u_2, \sigma_2)) \quad (\text{B.14})$$

$$u_4 = u^t + \Delta t (F_1(\sigma_3)) \quad \sigma_4 = \sigma^t + \Delta t (F_2(u_3, \sigma_3)). \quad (\text{B.15})$$

In standard SPH, Eqs. (B.12)–(B.15) are spatially resolved at each calculation step by calculating (B.8) and (B.9) at each node. In Stress-Particle SPH the stress is updated on the stress-points, and therefore Eqs. (B.9) and (B.5) are calculated on the stress-points.

## Appendix C. CSPM Gradient normalisation

A corrective term can be multiplied to the smoothing kernel to improve the accuracy of the SPH approximation [67,68]. The Corrective Smoothed Particle Method (CSPM) [69] increases the accuracy of the kernel via a normalisation procedure, which is based on a Taylor series expansion of the SPH equations. In one dimension, the Taylor series expansion of a function  $f(x)$  around a discrete point  $x_i$  is

$$f(x) = f_i + (x - x_i) \frac{\partial f_i}{\partial x} + \frac{(x - x_i)^2}{2!} \frac{\partial^2 f_i}{\partial x^2} + \dots, \quad (\text{C.1})$$

where  $f_i = f(x_i)$ . To derive the corrective term for CSPM, Eq. (C.1) is multiplied by the SPH kernel and integrated over the whole domain:

$$\begin{aligned} \int f(x) W_i(x) dx &= f_i \int W_i(x) dx + \frac{\partial f_i}{\partial x} \int (x - x_i) W_i(x) dx \\ &\quad + \frac{1}{2} \frac{\partial^2 f_i}{\partial x^2} \int (x - x_i)^2 W_i(x) dx + \dots \end{aligned} \quad (\text{C.2})$$

The differential terms are neglected, and (C.2) is rearranged to obtain the CSPM integral approximation for  $f_i$ :

$$f_i = \frac{\int f(x) W_i(x) dx}{\int W_i(x) dx}, \quad (\text{C.3})$$

which has a higher accuracy than the classic SPH approximation, particularly in the regions of the boundary. In two dimensions, the particle approximation of a function with the CSPM normalisation is

$$f_i = \frac{\sum_{j=1}^N \frac{m_j}{\rho_j} f(\mathbf{x}_j) W_{ij}}{\sum_{j=1}^N \frac{m_j}{\rho_j} W_{ij}}. \quad (\text{C.4})$$

The derivative of a function with the CSPM normalisation is derived by replacing the kernel with the kernel derivative in (C.2), and neglecting those that are of second order and higher. The resulting equation is then rearranged in terms of the gradient of  $f$ . In two dimensions, the derivation of the corresponding particle approximation requires the inversion of a  $2 \times 2$  matrix. The final result is

$$\left( \frac{\partial f}{\partial x} \right)_i = A_{11,i}^{-1} \sum_{j=1}^N \frac{m_j}{\rho_j} (f(\mathbf{x}_j) - f(\mathbf{x}_i)) \frac{\partial W_{ij}}{\partial x} + A_{12,i}^{-1} \sum_{j=1}^N \frac{m_j}{\rho_j} (f(\mathbf{x}_j) - f(\mathbf{x}_i)) \frac{\partial W_{ij}}{\partial y}, \quad (\text{C.5})$$

$$\left( \frac{\partial f}{\partial y} \right)_i = A_{21,i}^{-1} \sum_{j=1}^N \frac{m_j}{\rho_j} (f(\mathbf{x}_j) - f(\mathbf{x}_i)) \frac{\partial W_{ij}}{\partial x} + A_{22,i}^{-1} \sum_{j=1}^N \frac{m_j}{\rho_j} (f(\mathbf{x}_j) - f(\mathbf{x}_i)) \frac{\partial W_{ij}}{\partial y}, \quad (\text{C.6})$$

where

$$\mathbf{A}_i = \begin{pmatrix} \sum_{j=1}^N \frac{m_j}{\rho_j} (x_j - x_i) \frac{\partial W_{ij}}{\partial x} & \sum_{j=1}^N \frac{m_j}{\rho_j} (x_j - x_i) \frac{\partial W_{ij}}{\partial y} \\ \sum_{j=1}^N \frac{m_j}{\rho_j} (y_j - y_i) \frac{\partial W_{ij}}{\partial x} & \sum_{j=1}^N \frac{m_j}{\rho_j} (y_j - y_i) \frac{\partial W_{ij}}{\partial y} \end{pmatrix} \quad (\text{C.7})$$

For small deformation problems, the appropriate boundary conditions can be applied directly onto the SPH nodes and the CSPM normalisation can be included to improve the accuracy of the calculation in this area [29,31,70].

## Appendix D. Boundary repulsive force

A boundary repulsive force, introduced by Monaghan [50], can be included in SPH to prevent the interior particles from penetrating the boundary. In the classic repulsive force approach, the force is highly repulsive, which can cause unrealistic disturbances in the flow. A ‘soft’ repulsive force was later introduced that prevents particle penetration without obviously disturbing the interior particles [58]. The force  $\hat{\mathbf{F}}_{ij}$  is applied to all nodes that interact with the repulsive boundary particles, and is included in the SPH momentum equation:

$$\frac{D\mathbf{u}_i}{Dt} = \sum_{j=1}^N m_j \left( \frac{\mathbf{f}_i^\sigma}{\rho_i^2} + \frac{\mathbf{f}_j^\sigma}{\rho_j^2} + \Pi_{ij} \mathbf{I} \right) \nabla \cdot W_{ij} + \hat{\mathbf{F}}_{ij} + \mathbf{b}_i, \quad (\text{D.1})$$

The force is defined by the following equations:

$$\hat{\mathbf{F}}_{ij} = \sum_{j=1}^N 0.01c^2 \chi \cdot \hat{f}(\gamma) \frac{\mathbf{x}_{ij}}{r^2}, \quad (\text{D.2})$$

$$\chi = \begin{cases} 1 - \frac{r}{1.5\Delta x}, & 0 \leq r < 1.5\Delta x \\ 0, & r \geq 1.5\Delta x, \end{cases} \quad (\text{D.3})$$

$$\gamma = \frac{r}{0.75h_{ij}}, \quad (\text{D.4})$$

$$\hat{f}(\gamma) = \begin{cases} \frac{2}{3}, & 0 < \gamma \leq \frac{2}{3} \\ (2\gamma - 1.5\gamma^2), & \frac{2}{3} < \gamma \leq 1 \\ 0.5(2 - \gamma)^2, & 1 < \gamma < 2 \\ 0, & \gamma \geq 2, \end{cases} \quad (\text{D.5})$$

where  $r$  is the distance between two particles. Combined with dummy nodes, the soft repulsive force defined by Eqs. (D.2) to (D.5) has been applied to simulations of water flow [58] and the propagation of a Bingham material [71].

## Appendix E. Artificial stress

The concept of an artificial repulsive force within SPH was first introduced by Monaghan [30] to combat the tensile instability problem, and later extended to elastic materials by Gray et al. [72]. The artificial force was defined to introduce a short-range repulsive force between two particles, that increases as the distance between them decreases. This process has the purpose of preventing two particles from clumping together, and was shown to introduce minimal long-wavelength errors. The development of the method was motivated by the idea that SPH particles behave as atoms, with the artificial force acting as an atomic force. In the extension to elastic materials, an *artificial stress* is activated in the regions that are subject to a tensile stress. In the same way as for the artificial force, the artificial stress acts to prevent particles from becoming too close to one another. The artificial stress is included in the SPH momentum equation:

$$\frac{D\mathbf{u}_i}{Dt} = \sum_{j=1}^N m_j \left( \frac{\mathbf{f}_i^r}{\rho_i^2} + \frac{\mathbf{f}_j^r}{\rho_j^2} + \Pi_{ij} \mathbf{I} + f_{ij}^n (\mathbf{R}_i + \mathbf{R}_j) \right) \nabla \cdot W_{ij} + \mathbf{b}_i, \quad (\text{E.1})$$

where  $f_{ij}$  is the repulsive term, defined as

$$f_{ij} = \frac{W_{ij}}{W(\Delta x, h_s)}. \quad (\text{E.2})$$

Eq. (E.2) was defined to ensure that the artificial stress decreases as the particle separation increases, where  $W(\Delta x, h_s)$  is constant for a constant smoothing length. The exponent  $n$  in (E.1) is a model parameter. Bui et al. [20] used a value of  $n = 2.5$  in the application of the artificial stress method to an elastoplastic soil. The term  $\mathbf{R}$  in (E.1) is the artificial stress tensor, which is defined as follows:

$$R_{xx} = R'_{xx} \cos^2 \theta + R'_{yy} \sin^2 \theta \quad (\text{E.3})$$

$$R_{yy} = R'_{xx} \sin^2 \theta + R'_{yy} \cos^2 \theta \quad (\text{E.4})$$

$$R_{xy} = (R'_{xx} - R'_{yy}) \sin \theta \cos \theta, \quad (\text{E.5})$$

where  $\theta$  is defined as

$$\tan 2\theta = \frac{2\sigma_{xy}}{\sigma_{xx} - \sigma_{yy}}. \quad (\text{E.6})$$

In (E.3)–(E.5),  $R'_{\alpha\beta}$  is the artificial stress tensor in the principle coordinate system  $(x', y')$ . The principle artificial stress term is defined according to the components of the principle stress:

$$R'_{xx} = \begin{cases} -\epsilon \frac{\sigma'_{xx}}{\rho^2} & \text{if } \sigma'_{xx} > 0 \\ 0 & \text{if } \sigma'_{xx} \leq 0, \end{cases} \quad (\text{E.7})$$

where  $0 < \epsilon < 1$  is a constant parameter defining the magnitude of the repulsive force acting on the particles. Gray et al. [72] found  $\epsilon = 0.3$  to provide optimum results in the simulations of elastic solids, while Bui et al. [20] found that a value of  $\epsilon = 0.5$  was essential to remove the instabilities in a cohesive elastoplastic soil. The terms  $R'_{yy}$  and  $R'_{xy}$  are defined by replacing the subscript  $xx$  with  $yy$  or  $xy$  in (E.7). The principle stress  $\sigma'$  is related to the reference stress  $\sigma$  as

$$\sigma'_{xx} = \cos^2 \theta \sigma_{xx} + 2 \cos \theta \sin \theta \sigma_{xy} + \sin^2 \theta \sigma_{yy} \quad (\text{E.8})$$

$$\sigma'_{yy} = \sin^2 \theta \sigma_{xx} - 2 \cos \theta \sin \theta \sigma_{xy} + \cos^2 \theta \sigma_{yy}. \quad (\text{E.9})$$

When applicable, we use parameter values of  $n = 2.5$  and  $\epsilon = 0.5$  in the current work (to coincide with Bui et al. [20]).

## Appendix F. The effect of XSPH on the stress-particle SPH method

When the Stress-Particle SPH method was first applied to large displacement problems we found that the particles formed anisotropic structures due to the accuracy of the scheme (see Section 4.3.1). It was shown by Oger et al. [63]

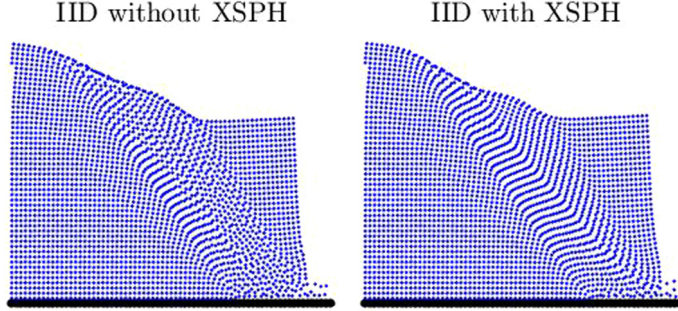


**Fig. 21.** The node positions at the front of the material at  $t = 2$  s, for the cohesive soil failure, calculated with configuration IID (see Fig. 13) of the updated Stress-Particle SPH model. The results show the effect of updating the node positions with XSPH.

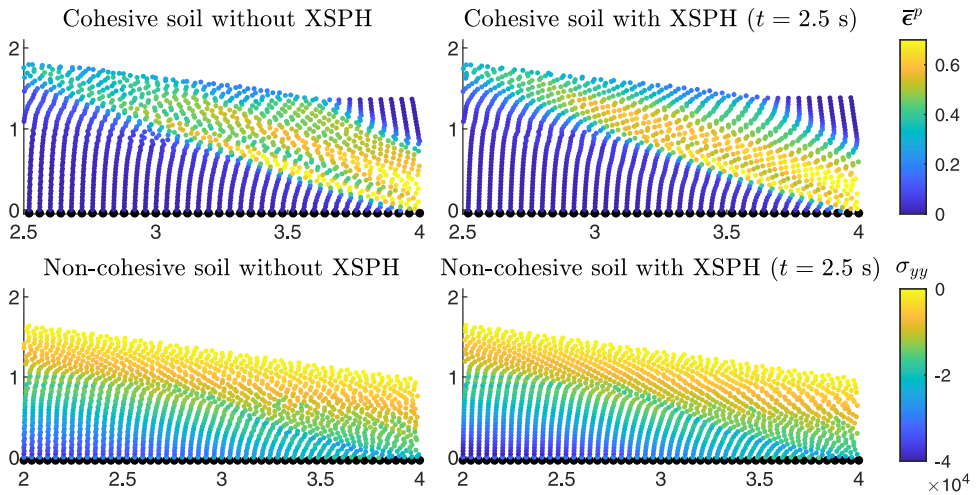


**Fig. 22.** The final node positions for the cohesive and non-cohesive soil problems, simulated with the velocity vector approach. The nodes are coloured by deviatoric plastic strain  $\bar{\epsilon}^p$  (dimensionless) and vertical stress  $\sigma_{yy}$  (Pa). The results are shown with and without XSPH for a section of the material.

that the presence of anisotropic structures in SPH can lead to particle disordering, which is potentially detrimental to SPH simulations. We therefore utilised the XSPH method [65] to reduce particle disordering, which updates each node with a velocity that is representative of the average velocity in its neighbourhood. We found that the XSPH method is capable of reducing particle disordering in Stress-Particle SPH (with the classic configuration, see Fig. 11), and it was included in all subsequent simulations. However, the XSPH method itself has stabilising effects. We here provide some results from the updated Stress-Particle SPH model (see Section 5) without XSPH, to distinguish the advantages of including stress-points within SPH from those of XSPH.

Fig. 21 shows the results of the cohesive soil calculated with the improved Stress-Particle SPH model, with and without XSPH. Note that XSPH is used to update the node positions, while the stress-points are defined to follow each node as described in Section 5. The results provided in Fig. 21 were calculated using configuration IID (see Fig. 13), which was shown to be most effective in Section 5. It can be seen that when XSPH is not utilised, the overall dynamics of the cohesive soil are captured well, and the non-physical material fractures have been eliminated. However, some particle disordering is noticeable when XSPH is not included — this has not affected our results overall, but has the potential to disrupt SPH simulations in general [63]. When XSPH is included, the particles have formed smooth trajectories that align with the direction of flow throughout the entire material. The same can be said of the velocity vector approach when considering the effect of XSPH on the simulation results (see Fig. 22). We can therefore conclude that although XSPH complements the Stress-Particle SPH method, it is not essential for stable and accurate results.

## References

- [1] R.M. Iverson, M.E. Reid, R.G. LaHusen, Debris-flow mobilization from landslides, *Annu. Rev. Earth Planet. Sci.* 25 (1) (1997) 85–138.
- [2] G.B. Crosta, S. Imposimato, D. Roddeman, S. Chiesa, F. Moia, Small fast-moving flow-like landslides in volcanic deposits: the 2001 Las Colinas Landslide (El Salvador), *Eng. Geol.* 79 (3–4) (2005) 185–214.
- [3] W.-F. Chen, E. Mizuno, et al., *Nonlinear Analysis in Soil Mechanics*, Elsevier, 1990.
- [4] M. Pastor, M. Quecedo, O.C. Zienkiewicz, A mixed displacement-pressure formulation for numerical analysis of plastic failure, *Comput. Struct.* 62 (1) (1997) 13–23.
- [5] M. Pastor, T. Li, J.A. Fernández-Merodo, Stabilized finite elements for harmonic soil dynamics problems near the undrained-incompressible limit, *Soil Dyn. Earthq. Eng.* 16 (3) (1997) 161–171.
- [6] J. Eichenberger, M. Nuth, L. Laloui, Modeling landslides in partially saturated slopes subjected to rainfall infiltration, *Mech. Unsaturated Geomater.* (2013) 233–250.
- [7] L. Cascini, S. Cuomo, M. Pastor, C. Sacco, Modelling the post-failure stage of rainfall-induced landslides of the flow type, *Can. Geotech. J.* 50 (9) (2013) 924–934.
- [8] D.L. George, R.M. Iverson, A depth-averaged debris-flow model that includes the effects of evolving dilatancy II numerical predictions and experimental tests, *Proc. R. Soc. A Math. Phys. Eng. Sci.* 470 (2170) (2014) 20130820.
- [9] G.B. Crosta, S. Imposimato, D. Roddeman, Granular flows on erodible and non erodible inclines, *Granul. Matter* 17 (5) (2015) 667–685.
- [10] S. Li, W.K. Liu, Meshfree and particle methods and their applications, *Appl. Mech. Rev.* 55 (1) (2002) 1–34.
- [11] S. McDougall, O. Hungr, A model for the analysis of rapid landslide motion across three-dimensional terrain, *Can. Geotech. J.* 41 (6) (2004) 1084–1097.
- [12] M. Pastor, B. Haddad, G. Sorbino, S. Cuomo, V. Drempetic, A depth-integrated, coupled SPH model for flow-like landslides and related phenomena, *Int. J. Numer. Anal. Methods Geomech.* 33 (2) (2009) 143–172.
- [13] S. Bandara, K. Soga, Coupling of soil deformation and pore fluid flow using material point method, *Comput. Geotech.* 63 (2015) 199–214.
- [14] L. Calvo, B. Haddad, M. Pastor, D. Palacios, Runout and deposit morphology of Bingham fluid as a function of initial volume: implication for debris flow modelling, *Nat. Hazards* 75 (1) (2015) 489–513.
- [15] K. Soga, E. Alonso, A. Yerro, K. Kumar, S. Bandara, Trends in large-deformation analysis of landslide mass movements with particular emphasis on the material point method, *Géotechnique* (2015) 1–26.
- [16] C.T. Nguyen, C.T. Nguyen, H.H. Bui, Giang D. Nguyen, R. Fukagawa, A new SPH-based approach to simulation of granular flows using viscous damping and stress regularisation, *Landslides* 14 (1) (2017) 69–81.
- [17] R.A. Gingold, J.J. Monaghan, Smoothed particle hydrodynamics: theory and application to non-spherical stars, *Mon. Not. R. Astron. Soc.* 181 (3) (1977) 375–389.
- [18] L.B. Lucy, A numerical approach to the testing of the fission hypothesis, *Astron. J.* 82 (1977) 1013–1024.
- [19] M.B. Liu, G.R. Liu, Smoothed particle hydrodynamics (SPH): an overview and recent developments, *Arch. Comput. Methods Eng.* 17 (1) (2010) 25–76.
- [20] H.H. Bui, R. Fukagawa, K. Sako, S. Ohno, Lagrangian meshfree particles method (SPH) for large deformation and failure flows of geomaterial using elastic–plastic soil constitutive model, *Int. J. Numer. Anal. Methods Geomech.* 32 (12) (2008) 1537–1570.
- [21] B. Haddad, M. Pastor, D. Palacios, E. Muñoz-Salinas, A SPH depth integrated model for Popocatépetl 2001 lahar (Mexico): sensitivity analysis and runout simulation, *Eng. Geol.* 114 (3) (2010) 312–329.
- [22] H.H. Bui, R. Fukagawa, K. Sako, J.C. Wells, Slope stability analysis and discontinuous slope failure simulation by elasto-plastic smoothed particle hydrodynamics (SPH), *Geotechnique* 61 (7) (2011) 565–574.
- [23] M. Pirulli, M. Pastor, Numerical study on the entrainment of bed material into rapid landslides, *Geotechnique* 62 (11) (2012) 959–972.
- [24] Z. Dai, Y. Huang, H. Cheng, Q. Xu, 3D numerical modeling using smoothed particle hydrodynamics of flow-like landslide propagation triggered by the 2008 Wenchuan earthquake, *Eng. Geol.* 180 (2014) 21–33.
- [25] G. Maenchen, S. Sack, The TENSOR code, Technical Report, California Univ, Livermore Lawrence Radiation Lab, 1963.
- [26] J.W. Swegle, S.W. Attaway, M.W. Heinstein, F.J. Mello, D.L. Hicks, An analysis of smoothed particle hydrodynamics, Sandia National Labs, Albuquerque, New Mexico (United States), 1994.
- [27] T. Belytschko, Y. Guo, W.K. Liu, S.P. Xiao, A unified stability analysis of meshless particle methods, *Internat. J. Numer. Methods Engrg.* 48 (9) (2000) 1359–1400.
- [28] Y. Vidal, J. Bonet, A. Huerta, Stabilized updated Lagrangian corrected SPH for explicit dynamic problems, *Internat. J. Numer. Methods Engrg.* 69 (13) (2007) 2687–2710.
- [29] T. Blanc, The Runge-Kutta Taylor-SPH model, a new improved model for soil dynamics problems (Ph.D. thesis), Universidad Politécnica de Madrid, 2011.
- [30] J.J. Monaghan, SPH Without a tensile instability, *J. Comput. Phys.* 159 (2) (2000) 290–311.
- [31] T. Blanc, M. Pastor, A stabilized smoothed particle hydrodynamics, Taylor-Galerkin algorithm for soil dynamics problems, *Int. J. Numer. Anal. Methods Geomech.* 37 (1) (2013) 1–30.
- [32] R. Xu, P. Stansby, D. Laurence, Accuracy and stability in incompressible SPH (ISPH) based on the projection method and a new approach, *J. Comput. Phys.* 228 (18) (2009) 6703–6725.
- [33] X. Xu, P. Yu, A technique to remove the tensile instability in weakly compressible SPH, *Comput. Mech.* 62 (5) (2018) 963–990.
- [34] P.N. Sun, A. Colagrossi, S. Marrone, M. Antuono, A.-M. Zhang, A consistent approach to particle shifting in the  $\delta$ -Plus-SPH model, *Comput. Methods Appl. Mech. Engrg.* 348 (2019) 912–934.
- [35] S. Patankar, *Numerical Heat Transfer and Fluid Flow*, CRC press, 1980.

- [36] C.T. Dyka, P.W. Randles, R.P. Ingel, An approach for tension instability in smoothed particle hydrodynamics (SPH), *Comput. Struct.* 57 (4) (1995) 573–580.
- [37] P. Randles, L. Libersky, Normalized SPH with stress points, *Internat. J. Numer. Methods Engrg.* 48 (10) (2000) 1445–1462.
- [38] R. Vignjevic, J. Campbell, L. Libersky, A treatment of zero-energy modes in the smoothed particle hydrodynamics method, *Comput. Methods Appl. Mech. Engrg.* 184 (1) (2000) 67–85.
- [39] T. Rabczuk, T. Belytschko, Cracking particles: a simplified meshfree method for arbitrary evolving cracks, *Internat. J. Numer. Methods Engrg.* 61 (13) (2004) 2316–2343.
- [40] T. Rabczuk, T. Belytschko, S.P. Xiao, Stable particle methods based on Lagrangian kernels, *Comput. Methods Appl. Mech. Engrg.* 193 (12–14) (2004) 1035–1063.
- [41] T. Rabczuk, P.M.A. Areias, T. Belytschko, A simplified mesh-free method for shear bands with cohesive surfaces, *Internat. J. Numer. Methods Engrg.* 69 (5) (2007) 993–1021.
- [42] T. Rabczuk, T. Belytschko, A three-dimensional large deformation meshfree method for arbitrary evolving cracks, *Comput. Methods Appl. Mech. Engrg.* 196 (29–30) (2007) 2777–2799.
- [43] T. Rabczuk, R. Gracie, J.-H. Song, T. Belytschko, Immersed particle method for fluid–structure interaction, *Internat. J. Numer. Methods Engrg.* 81 (1) (2010) 48–71.
- [44] J. Sanchez, P. Randles, Dynamic failure simulation of quasi-brittle material in dual particle dynamics, *Internat. J. Numer. Methods Engrg.* 91 (11) (2012) 1227–1250.
- [45] J. Sanchez, P. Randles, A quasi-static dual particle method for solids based on dual particle dynamics, *Internat. J. Numer. Methods Engrg.* 94 (2) (2013) 183–203.
- [46] P. Perzyna, Fundamental problems in viscoplasticity, in: *Advances in Applied Mechanics*, vol. 9, Elsevier, 1966, pp. 243–377.
- [47] G.C. Johnson, D.J. Bammann, A discussion of stress rates in finite deformation problems, *Int. J. Solids Struct.* 20 (8) (1984) 725–737.
- [48] J.K. Dienes, On the analysis of rotation and stress rate in deforming bodies, *Acta Mech.* 32 (4) (1979) 217–232.
- [49] M.B. Liu, G.R. Liu, K.Y. Lam, Constructing smoothing functions in smoothed particle hydrodynamics with applications, *J. Comput. Appl. Math.* 155 (2) (2003) 263–284.
- [50] J.J. Monaghan, Simulating free surface flows with SPH, *J. Comput. Phys.* 110 (2) (1994) 399–406.
- [51] M. Gómez-Gesteira, B.D. Rogers, R.A. Dalrymple, A.J. Crespo, State-of-the-art of classical SPH for free-surface flows, *J. Hydraul. Res.* 48 (S1) (2010) 6–27.
- [52] J. Von Neumann, R.D. Richtmyer, A method for the numerical calculation of hydrodynamic shocks, *J. Appl. Phys.* 21 (3) (1950) 232–237.
- [53] J.J. Monaghan, On the problem of penetration in particle methods, *J. Comput. Phys.* 82 (1) (1989) 1–15.
- [54] I. Flammer, A. Blum, A. Leiser, P. Germann, Acoustic assessment of flow patterns in unsaturated soil, *J. Appl. Geophys.* 46 (2) (2001) 115–128.
- [55] F. Adamo, G. Andria, F. Attivissimo, N. Giaquinto, An acoustic method for soil moisture measurement, *IEEE Trans. Instrum. Meas.* 53 (4) (2004) 891–898.
- [56] J.K. Chen, J.E. Beraun, A generalized smoothed particle hydrodynamics method for nonlinear dynamic problems, *Comput. Methods Appl. Mech. Engrg.* 190 (1–2) (2000) 225–239.
- [57] J.P. Morris, P.J. Fox, Y. Zhu, Modeling low Reynolds number incompressible flows using SPH, *J. Comput. Phys.* 136 (1) (1997) 214–226.
- [58] M.B. Liu, J.R. Shao, J.Z. Chang, On the treatment of solid boundary in smoothed particle hydrodynamics, *Sci. China Technol. Sci.* 55 (1) (2012) 244–254.
- [59] H.H. Bui, R. Fukagawa, An improved SPH method for saturated soils and its application to investigate the mechanisms of embankment failure: case of hydrostatic pore-water pressure, *Int. J. Numer. Anal. Methods Geomech.* 37 (1) (2013) 31–50.
- [60] M. Mabsout, M.I. Herreros, Runge–Kutta vs Taylor-SPH: Two time integration schemes for SPH with application to soil dynamics, *Appl. Math. Model.* 37 (5) (2013) 3541–3563.
- [61] L.J. Sluys, Wave propagation, localisation and dispersion in softening solids (Ph.D. thesis), Delft University of Technology, 1992.
- [62] M. Antuono, B. Bouscasse, A. Colagrossi, S. Marrone, A measure of spatial disorder in particle methods, *Comput. Phys. Comm.* 185 (10) (2014) 2609–2621.
- [63] G. Oger, S. Marrone, D. Le Touzé, M. De Leffe, SPH accuracy improvement through the combination of a quasi-Lagrangian shifting transport velocity and consistent ALE formalisms, *J. Comput. Phys.* 313 (2016) 76–98.
- [64] N.J. Quinlan, M. Basa, M. Lastiwka, Truncation error in mesh-free particle methods, *Internat. J. Numer. Methods Engrg.* 66 (13) (2006) 2064–2085.
- [65] J.J. Monaghan, Smoothed particle hydrodynamics, *Ann. Rev. Astron. Astrophys.* 30 (1) (1992) 543–574.
- [66] W.-F. Chen, *Limit Analysis and Soil Plasticity*, Elsevier, 2013.
- [67] W.K. Liu, S. Jun, Y.F. Zhang, Reproducing kernel particle methods, *Internat. J. Numer. Methods Fluids* 20 (8–9) (1995) 1081–1106.
- [68] S. Li, W.K. Liu, Reproducing kernel hierarchical partition of unity, part I – formulation and theory, *Internat. J. Numer. Methods Engrg.* 45 (3) (1999) 251–288.
- [69] J.K. Chen, J.E. Beraun, T.C. Carney, A corrective smoothed particle method for boundary value problems in heat conduction, *Internat. J. Numer. Methods Engrg.* 46 (2) (1999) 231–252.
- [70] T. Blanc, M. Pastor, A stabilized Runge–Kutta, Taylor smoothed particle hydrodynamics algorithm for large deformation problems in dynamics, *Internat. J. Numer. Methods Engrg.* 91 (13) (2012) 1427–1458.
- [71] M. Hu, M.B. Liu, M.W. Xie, G.R. Liu, Three-dimensional run-out analysis and prediction of flow-like landslides using smoothed particle hydrodynamics, *Environ. Earth Sci.* 73 (4) (2015) 1629–1640.
- [72] J.P. Gray, J.J. Monaghan, R.P. Swift, SPH elastic dynamics, *Comput. Methods Appl. Mech. Engrg.* 190 (49–50) (2001) 6641–6662.